Japan; the Program for Promotion of Fundamental Studies in Health Science of the Organization for Pharmaceutical Safety and Research of Japan; and a Grant-in-Aid for Scientific Research from the Ministry of Education, Culture, Sports, Science and Technology (MEXT) of Japan

Conflicts of interest

The authors have no conflicts of interest to disclose.

Open Access

References

1. McCord ME, Bacharach SL, Bonow RO, Dilsizian V, Cuocolo A, Freedman N. Misalignment between PET transmission and emission scans: Its effect on myocardial imaging. J Nucl Med 1992;33:1209-14.
2. Bacharach SL, Douglas MA, Carson RE, Kalkowski PJ, Freedman NM, Perrone-Filardi P, et al. Three-dimensional registration of cardiac positron emission tomography attenuation scans. J Nucl Med 1993;34:311-21.
3. Naum A, Laaksonen MS, Tuunanen H, Oikonen Va, Teräs M, Kemppainen J, et al. Motion detection and correction for dynamic (15)O-water myocardial perfusion PET studies. Eur J Nucl Med Mol Imaging 2005;32:1378-83.
4. Iida H, Kanno I, Takahashi A, Miura S, Murakami M, Takahashi K, et al. Measurement of absolute myocardial blood flow with H215O and dynamic positron-emission tomography. Strategy for quantification in relation to the partial-volume effect. Circulation 1988;78:104-15. (Erratum in: Circulation 1988;78:1078).
5. Iida H, Rhodes CG, de Silva R, Yamamoto Y, Araujo LI, Maseri A, et al. Myocardial tissue fraction-correction for partial volume effects and measure of tissue viability. J Nucl Med 1991;32:2169-75.
6. Iida H, Rhodes CG, de Silva R, Araujo LI, Bloomfield PM, Lammertsma AA, et al. Use of the left ventricular time-activity curve as a noninvasive input function in dynamic oxygen-15-water positron emission tomography. J Nucl Med 1992;33:1669-77.
7. Yamamoto Y, de Silva R, Rhodes CG, Araujo LI, Iida H, Rechavia E, et al. A new strategy for the assessment of viable myocardium and regional myocardial blood flow using 15O-water and dynamic positron emission tomography. Circulation 1992;86:167-78.
8. de Silva R, Yamamoto Y, Rhodes CG, Iida H, Nihoyannopoulos P, Davies GJ, et al. Preoperative prediction of the outcome of coronary revascularization using positron emission tomography. Circulation 1992;86:1738-42.
9. Iida H, Rhodes CG, Araujo LI, Yamamoto Y, de Silva R, Maseri A, et al. Noninvasive quantification of regional myocardial metabolic rate for oxygen by use of $^{15}O_2$ inhalation and positron emission tomography. Theory, error analysis, and application in humans. Circulation 1996;94:792-807.
10. Chareonthaitawee P, Kaufmann PA, Rimoldi O, Camici PG. Heterogeneity of resting and hyperemic myocardial blood flow in healthy humans. Cardiovasc Res 2001;50:151-61.
11. Knaapen P, Boellaard R, Götte MJ, van der Weerdt AP, Visser CA, Lammertsma AA, et al. The perfusable tissue index: A marker of myocardial viability. J Nucl Cardiol 2003;10:684-91.
12. Knaapen P, Boellaard R, Götte MJ, Dijkmans PA, van Campen LM, de Cock CC, et al. Perfusable tissue index as a potential marker of fibrosis in patients with idiopathic dilated cardiomyopathy. J Nucl Med 2004;45:1299-304.
13. Koshino K, Watabe H, Hasegawa S, Hayashi T, Hatazawa J, Iida H. Development of motion correction technique for cardiac 15O-water PET study using an optical motion tracking system. Ann Nucl Med 2010;24:1-11.
14. Miyagawa S, Matsumiya G, Funatsu T, Yoshitatsu M, Sekiya N, Fukui S, et al. Combined autologous cellular cardiomyoplasty using skeletal myoblasts and bone marrow cells for human ischemic cardiomyopathy with left ventricular assist system implantation: Report of a case. Surg Today 2009;39:133-6.
15. Miyagawa S, Saito A, Sakaguchi T, Yoshikawa Y, Yamauchi T, Imanishi Y, et al. Impaired myocardium regeneration with skeletal cell sheets—a preclinical trial for tissue-engineered regeneration therapy. Transplantation 2010;90:364-72.
16. Iida H, Miura S, Kanno I, Ogawa T, Uemura K. A new PET camera for noninvasive quantitation of physiological functional parametric images: HEADTOME-V-Dual. In: Myers R, Cunningham V, Bailey D, editors. Quantification of brain function using PET. London: Academic Press; 1996. p. 57-61.
17. Watabe H, Sato N, Kondoh Y, Fulton RR, Iida H. Correction of head movement using optical motion tracking system during PET study with rhesus monkey. In: Senda M, Kimura Y, Herscovitch P, editors. Brain imaging using PET. London: Academic Press; 2002. p. 1-8.
18. Woo SK, Watabe H, Yong C, Kim KM, Choon C, Bloomfield PM, et al. Sinogram-based motion correction of PET images using optical motion tracking system and list-mode data acquisition. IEEE Trans Nucl Sci 2004;51:782-8.
19. Katoh C, Morita K, Shiga T, Kubo N, Nakada K, Tamaki N, et al. Improvement of algorithm for quantification of regional myocardial blood flow using 15O-water with PET. J Nucl Med 2004;45:1908-16.
20. Watabe H, Jino H, Kawachi N, Teramoto N, Hayashi T, Ohta Y, et al. Parametric imaging of myocardial blood flow with 15O-water and PET using the basis function method. J Nucl Med 2005;46:1219-24.
21. Lubberink M, Harms HJ, Halbmeijer R, de Haan S, Knaapen P, Lammertsma AA. Low-dose quantitative myocardial blood flow imaging using 15O-water and PET without attenuation correction. J Nucl Med 2010;51:575-80.
22. Goetze S, Brown TL, Lavely WC, Zhang Z, Bengel FM. Attenuation correction in myocardial perfusion SPECT/CT: Effects of misregistration and value of reregistration. J Nucl Med 2007;48:1090-5.
23. Martinez-Möller A, Souvatzoglou M, Navab N, Schwaiger M, Nekolla SG. Artifacts from misaligned CT in cardiac perfusion PET/CT studies: Frequency, effects, and potential solutions. J Nucl Med 2007;48:188-93.
24. Nesterov SV, Han C, Mäki M, Kajander S, Naum AG, Helenius H, et al. Myocardial perfusion quantitation with 15O-labelled water PET: High reproducibility of the new cardiac analysis software (Carimas). Eur J Nucl Med Mol Imaging 2009;36:1594-602.

ARTICLE IN PRESS

Available online at www.sciencedirect.com

SciVerse ScienceDirect

Nuclear Medicine and Biology xx (2012) xxx–xxx

NUCLEAR MEDICINE — AND — BIOLOGY

www.elsevier.com/locate/nucmedbio

Quantification of regional cerebral blood flow in rats using an arteriovenous shunt and micro-PET

Takayuki Ose[a], Hiroshi Watabe[b], Takuya Hayashi[a,*], Nobuyuki Kudomi[c], Masaaki Hikake[d,e], Hajime Fukuda[d,e], Noboru Teramoto[f], Yasuyoshi Watanabe[a], Hirotaka Onoe[a], Hidehiro Iida[e]

[a]*Functional Probe Research Laboratory, RIKEN Center for Molecular Imaging Science, Chuo-ku, Kobe 650-0047, Japan*
[b]*Faculty of Molecular Imaging in Medicine, Osaka University Graduate School of Medicine, Suita, Osaka 565-0871, Japan*
[c]*Department of Clinical Radiology, Kagawa University Hospital, Miki-cho, Kita-gun, Kagawa 761-0793, Japan*
[d]*Molecular Imaging Labo Inc., Suita, Osaka 564-0053, Japan*
[e]*Department of Investigative Radiology, Advanced Medical-Engineering Center, National Cerebral and Cardiovascular Center-Research Institute, Suita, Osaka 565-8565, Japan*
[f]*Division of Cardiovascular Surgery Department of Surgery Osaka University Graduate School of Medicine, Suita, Osaka 565-0871, Japan*

Received 27 April 2011; received in revised form 14 November 2011; accepted 24 November 2011

Abstract

Introduction: Measurement of regional cerebral blood flow (rCBF) in rodents can provide knowledge of pathophysiology of the cerebral circulation, but generally requires blood sampling for analysis during positron emission tomography (PET). We therefore tested the feasibility of using an arteriovenous (AV) shunt in rats for less invasive blood analysis.
Methods: Six anesthetized rats received $[^{15}O]H_2O$ and $[^{15}O]CO$ PET scans with their femoral artery and vein connected by an AV shunt, the activity within which was measured with a germanium ortho-oxysilicate scintillation detector. The $[^{15}O]H_2O$ was intravenously injected either at a faster or slower injection rate, while animals were placed either with their head or heart centered in the gantry. The time–activity curve (TAC) from the AV shunt was compared with that from the cardiac ventricle in PET image. The rCBF values were calculated by a nonlinear least-square method using the dispersion-corrected AV-shunt TAC as an input.
Results: The AV-shunt TAC had higher signal-to-noise ratio, but also had delay and dispersion compared with the image-derived TAC. The delay time between the AV-shunt TAC and image-based TAC ranged from 11 to 21 s, while the dispersion was estimated to be ~5 s as a time constant of the dispersion model of exponential function, and both were properly corrected. In a steady-state condition of $[^{15}O]CO$ PET, the blood activity concentration by AV-shunt TAC was also comparable in height with the image-based TAC corrected for partial volume. Whole-brain CBF values measured by $[^{15}O]H_2O$ were 0.37±0.04 (mean±S.D.) ml/g/min, partition coefficient was 0.73±0.04 ml/g, and the CBF varied in a linear relationship with partial pressure of carbon dioxide during each scan.
Conclusions: The AV-shunt technique allows less invasive, quantitative and reproducible measurement of rCBF in $[^{15}O]H_2O$ PET studies in rats than direct blood sampling and radioassay.

Keywords: Positron emission tomography; Oxygen radioisotopes; Rats; Cerebral blood flow; AV shunt; CO_2

1. Introduction

Regional cerebral blood flow (rCBF) is one of the most frequently used clinically evaluable parameters for characterizing regional hemodynamic and/or functional status of the brain, and can be noninvasively measured by positron emission tomography (PET) using ^{15}O-labeled water [1]. The short physical half-life of ^{15}O (~2 min) also allows repeat measurements of rCBF under different conditions within a relatively short period of time. One of the concerns when measuring rodent rCBF using $[^{15}O]H_2O$ PET is blood sampling from an artery, which is needed to obtain the arterial input function and calculate rCBF. Owing to the small total volume of blood in rodents, withdrawal of blood

* Corresponding author. Tel.: +81 78 304 7121; fax: +81 78 304 7123.
E-mail address: takuya.hayashi@riken.jp (T. Hayashi).

0969-8051/$ – see front matter © 2011 Elsevier Inc. All rights reserved.
doi:10.1016/j.nucmedbio.2011.11.004

may alter the physiological conditions of the animals, resulting in instability or bias in the measured rCBF. An image-driven input function in rat PET, which derives time–activity curve (TAC) from a region of interest in the cardiac ventricle, may be a potential solution [2]. However, such image-based data may be compromised by statistical (i.e., count-related) 'noise' or biased by the partial volume effect; thus, it is not so simple to estimate arterial input function. Yee et al. recently proposed a model to estimate the input function in rats from the cardiac PET [^{15}O]H_2O image [2], but the model assumed multiple heuristic parameters and is thus difficult to validate.

The arteriovenous (AV)-shunt technique is one of the possible approaches to obtain the input function, and several studies have used this technique using radioactive tracers [3–6]. This technique involves placing a shunt between an artery and vein using a catheter and tube, in which blood activity concentration could be measured by an external detector. The advantages of the AV-shunt technique are high temporal resolution and no loss of blood during the PET study. However, there is concern of potential bias in the arterial input function, for example, due to time delay and dispersion, which may be augmented by a lengthy shunt. In addition, potential unstable flow resulting from blood clotting within the tube has not been well studied.

The aim of this study was to validate the arterial input function obtained by the AV shunt as a reference of image-based one and to quantify the rCBF of rats using [^{15}O]H_2O PET. For this purpose, we first evaluated the stability of blood flow velocity in the AV-shunt line by ultrasonography during the PET scans. Then, we separately performed two scans, one for the heart and the other for the brain, in each animal. The former scan was obtained to validate the shape of arterial input function from the AV shunt, and the latter for calculation of rCBF using the AV-shunt-based TAC. To validate the shape of the AV-shunt-derived blood TAC, the two different methods of injections (faster or slower) were performed. Thereafter, the delay and dispersion of the AV-shunt-based input function were evaluated by comparing with the input function from a region of interest in the left ventricle in the PET images. For the calculation of rCBF, the delay- and dispersion-corrected AV-shunt-derived TAC was used, and we investigated the relationship between the measured rCBF and arterial carbon dioxide partial pressure (pCO_2) during each measurement to confirm whether the current system reproduces the known physiological linear relationship between rCBF and pCO_2.

2. Material and methods

2.1. Overview of the study

Fig. 1 presents a schematic diagram of our experimental setup. To confirm the stability of the AV shunt during the PET scan, we continuously monitored the blood flow velocity in the AV-shunt line using ultrasonography. For injection of [^{15}O]H_2O, we tested two injection procedures, namely, faster and slower bolus injection, as shown in Fig. 1C. Fig. 2 shows our experimental protocol for PET scans. A total of three emission scans of [^{15}O]CO for heart, [^{15}O]H_2O for heart and [^{15}O]H_2O for brain were performed in each animal, with additional transmission scans for attenuation correction of 511 keV gamma rays. The cardiac [^{15}O]CO image was used to identify the cardiac ventricle to obtain image-based arterial TACs, while the cardiac [^{15}O]H_2O images were utilized to compare the shape of the arterial input function from the heart and from the AV-shunt line as well as to estimate the dispersion parameter of the input function from the AV shunt. [^{15}O]CO is known to label the red blood cells in the blood, and the specific activity of the supplied [^{15}O]CO was high enough to prevent side effects.

2.2. Animal preparation

Six male Sprague–Dawley rats (6 weeks old) were used in this study. Their body weight ranged from 257 to 319 g (mean±standard deviation, 283±22). The animals were maintained and handled in accordance with the *Guidelines for Proper Conduct of Animal Experiments* (June 1, 2006 Science Council of Japan). The study protocol was approved by the Laboratory Animal Welfare of the National Cardiovascular Center.

We performed all the experiments under deep anesthesia. The anesthesia was induced by intramuscular injection of ketamine (30–50 mg/kg) and xylazine (5–10 mg/kg). A rat was intubated for inhalation of [^{15}O]CO gas and for management of respiration using a respirator (SN-480-7, Shimano, Tokyo, Japan). Two 22-gauge needles were percutaneously inserted into the caudal veins and were attached to 25-cm-long polyethylene tubes for maintenance anesthesia using propofol (20–25 mg/kg/h) and for injection of [^{15}O]H_2O. The right femoral artery was catheterized with a polyethylene tube (PE50, inner diameter of 0.54 mm) for sampling blood for blood gas analysis and for monitoring heart rate and blood pressure using a physiological monitoring device (BSM-2391 Nihon Kohden, Tokyo, Japan). The left femoral artery and vein were also catheterized with PE50 tubes for the AV shunt. The length of the tubes was 55 and 35 cm for the left femoral artery and left femoral vein, respectively, and 10 cm of the ends of the two lines was connected to a thicker polyethylene tube (PE 100, inner diameter of 0.86 mm) to form the AV shunt and to allow passive blood flow dependent on the pressure gradient from artery to vein. The thicker part of the tube was used for monitoring blood flow by the ultrasonographic probe as described below, and a part of the arterial side of the PE50 tube (35–45 cm from the femoral artery) was used for online measurement of activity concentration using a Gd_2SiO_5:Ce (GSO) detector (GSO input function monitor system, Molecular Imaging Laboratory, Osaka, Japan) [7]. The GSO detector consists of two pairs of GSO crystals (20 mm×20 mm×12.9 mm for each) with photomultiplier tube

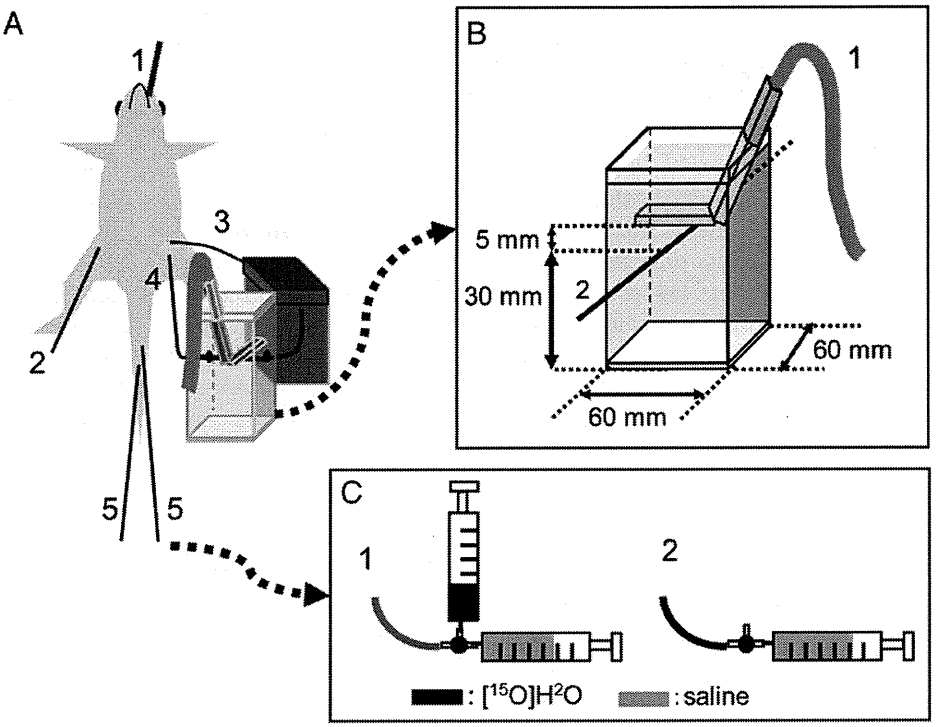

Fig. 1. A schematic diagram of the experimental setup. (A) Animal preparation: intubation for inhalation (1), blood catheter lines in the left femoral artery (3) and vein (4) for AV shunt, and in the right femoral artery (2) for monitoring heart pressure, and in two caudal veins (5), one for injection of $[^{15}O]H_2O$ and the other for infusion of anesthetics. (B) Measurements of blood flow velocity in the AV-shunt line by ultrasonography: the appliance consisted of an echo probe (1) and AV-shunt line (2), and the container was filled with water. The distance between the AV-shunt line and the echo probe was kept at 5 mm. (C) Two injection methods: faster bolus injection (1) and slower bolus injection (2). In the faster bolus injection, a solution of $[^{15}O]H_2O$ (volume of ~0.3 ml) in a 1-ml syringe was injected in a period of 15 s into the tail vein, and then the three-way stopcock was turned to the other syringe to flush through 0.7 ml of saline. In the slower bolus injection, $[^{15}O]H_2O$ (~0.3 ml) filled the venous catheter line before injection and was flushed through by 0.7±0.1 ml of saline in the syringe over a period of 30 s.

and coincidence circuits. A 2-cm-thick lead is utilized for shielding. The absolute sensitivity for PET tracers is approximately 7%.The total volume in the AV-shunt line was 0.26 ml (as a reference, the total amount of blood per body is ~20 ml). The AV-shunt line was coated with heparin to prevent clot formation. Soon after equipment setup, the animal was fixed in a supine position on the micro-PET imaging bed. A blood sample from the femoral artery was analyzed for pCO_2 using a blood gas analyzer (ABL-500, RADIOMETER, Tokyo, Japan). Body temperature was measured with a probe placed in the rectum, and kept at 36°C±1°C by using an infrared thermostat.

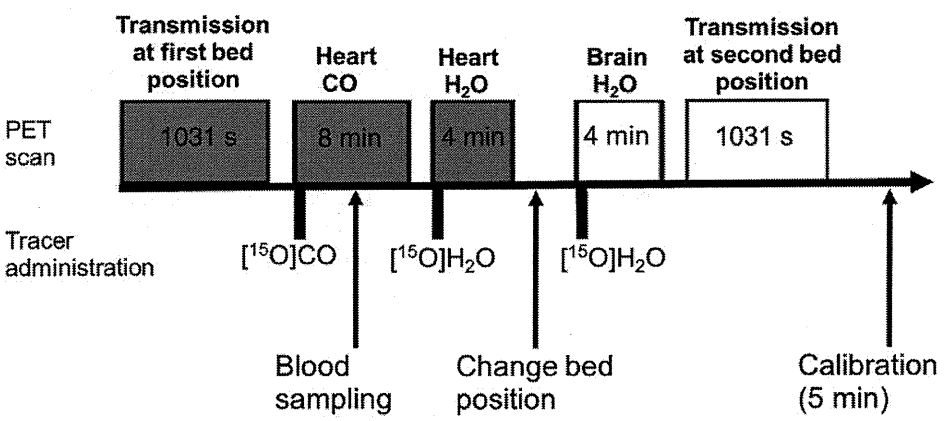

Fig. 2. Experimental protocol. The first three PET scans (gray) were performed for derivation of the cardiac ventricular TAC, while the latter two (white) were performed for brain imaging and the cerebral TAC. The activity concentration of the AV shunt was monitored and recorded to obtain the TAC during the PET scan.

2.3. Measurement of AV-shunt line blood flow velocity by ultrasonography

To confirm that blood constantly flows in the AV-shunt line, we performed measurements of blood flow velocity in three rats using a portable ultrasonographic device (LOGIQ BOOK XP, GE Healthcare UK Ltd., Buckinghamshire, UK) with a probe (i12L-RS, GE Healthcare UK Ltd., Buckinghamshire, UK). The AV-shunt line was placed 30 mm from the bottom of a box filled with water (Fig. 1B), and the distance between the line and the probe was kept at 5 mm. Blood flow velocity (cm/s) was monitored by the ultrasonographic probe during the experiment. The values of blood flow velocity measured by pulse Doppler were recorded twice during each emission scan. The velocity was scaled by the initial value measured before the PET scan of $[^{15}O]CO$ in the heart.

2.4. Injection methods

Intravenous injection of $[^{15}O]H_2O$ was performed in two ways, according to injection rate (faster, n=3 or slower, n=3) (Fig. 1C). In the faster bolus injection, a solution of $[^{15}O]H_2O$ (59±1.6 MBq, in a volume of ~0.3 ml) in a 1-ml syringe was injected in a period of 15 s into the tail vein, and then the three-way stopcock was turned to the other syringe to flush through 0.7 ml of saline. In the slower bolus injection, $[^{15}O]H_2O$ (~0.3 ml) filled the venous catheter line before injection and was flushed through by 0.7±0.1 ml of saline in the syringe over a period of 30 s. In both methods, the total injected radioactivity at the time of tracer injection was 68.6±3.3 MBq.

2.5. PET experiments

We used a PET scanner (micro-PET Focus 120, SIEMENS Healthcare USA Inc., Malvern, PA, USA) for imaging activity concentration distribution. This PET scanner is dedicated for small-animal use and has a transaxial field of view (FOV) of 10 cm and an axial FOV of 7.6 cm. The sensitivity and the spatial resolution at the center of the scanner are 7% and 1.18 mm full-width half-maximum, respectively [8]. All PET emission data were acquired in list mode.

For the scan protocol (Fig. 2), the animal was first positioned with its chest (heart) centered in the FOV of the PET scanner to scan the heart. After a transmission scan for a period of 1031 s using a $^{68}Ga/Ge$ pinpoint source, an emission scan was initiated immediately after completion of inhalation of $[^{15}O]CO$ (350±20 MBq/min) for 10 s and continued for a period of 8 min. A blood sample was taken from the femoral artery at 4–5 min after starting inhalation of $[^{15}O]CO$ and was radioassayed using a well counter (BeWell, Molecular Imaging Laboratory, Osaka, Japan). After radioactive decay, an emission scan for a period of 4 min was performed immediately after injection of $[^{15}O]H_2O$ by either faster or slower bolus injection. Then, the animal was repositioned with its head centered in the FOV of the PET scanner for brain scanning, and a 4-min emission scan was performed after injection of $[^{15}O]H_2O$ by either faster or slower bolus injection. The injection method of $[^{15}O]H_2O$ was the same as for the heart scan for each subject. A transmission scan was finally acquired for correction of attenuation. During PET scanning, activity concentration in the AV-shunt line was continuously recorded every second by the GSO detector. After all the PET scans, we removed the AV-shunt line from the animal, filled the line with saline containing $[^{15}O]H_2O$ of known activity concentration measured by the well counter, for cross-calibration of the GSO detector. The well counter was also calibrated to the PET scanner.

PET data, acquired in list mode, were sorted into multiple frames of 3D sinogram data. The emission data for $[^{15}O]CO$ consisted of 31 frames (18 frames×10 s, 12 frames×20 s, 1 frame×60 s), and for $[^{15}O]H_2O$ (in both heart and brain scans), 63 frames (30 frames×2 s, 30 frames×5 s, 3 frames×10 s). All sinogram data were reconstructed by a filtered back projection algorithm (a Ramp filter, cutoff frequency of 0.5 of the Nyquist frequency) with Fourier rebinning and with correction of attenuation using transmission data.

The TACs of arterial blood in the AV shunt were obtained from activity concentration data measured by the GSO detector, corrected for physical decay of ^{15}O and for cross-calibration between the GSO detector and the well counter.

2.6. Determination of image-derived TACs

To derive the image-based TAC, we identified the left ventricular blood pool from multiple PET images and derived time–activity concentration data from the H_2O PET scan [9]. To identify the region of blood pool, we subtracted the summed $[^{15}O]CO$ image from the summed $[^{15}O]H_2O$ image to generate an image that more clearly delineated the border of the myocardium and ventricle (Fig. 3A). A volume of interest (VOI) was defined by manually drawing the border of the ventricle, and the VOI was superimposed on the $[^{15}O]H_2O$ dynamic images to obtain the TAC. As shown in this figure, the initial phase of the $[^{15}O]H_2O$ image showed higher accumulation in the ventricle, while at the later equilibrium phase, the ventricular blood pool became indistinguishable from the myocardium, suggesting more homogenous activity concentration between these compartments at this phase. For the VOI analysis, we used the ASIPro VMimage analysis software (Concorde Micro systems, Knoxville, TN, USA).

2.7. Consistency of input functions obtained from the AV shunt and PET image

To compare the shape of the TACs from the AV-shunt technique and the PET image, we first derived an averaged TAC for each injection method (faster vs. slower) and measurement modality (AV shunt vs. image-derived). Averaging was performed across measurements and animals

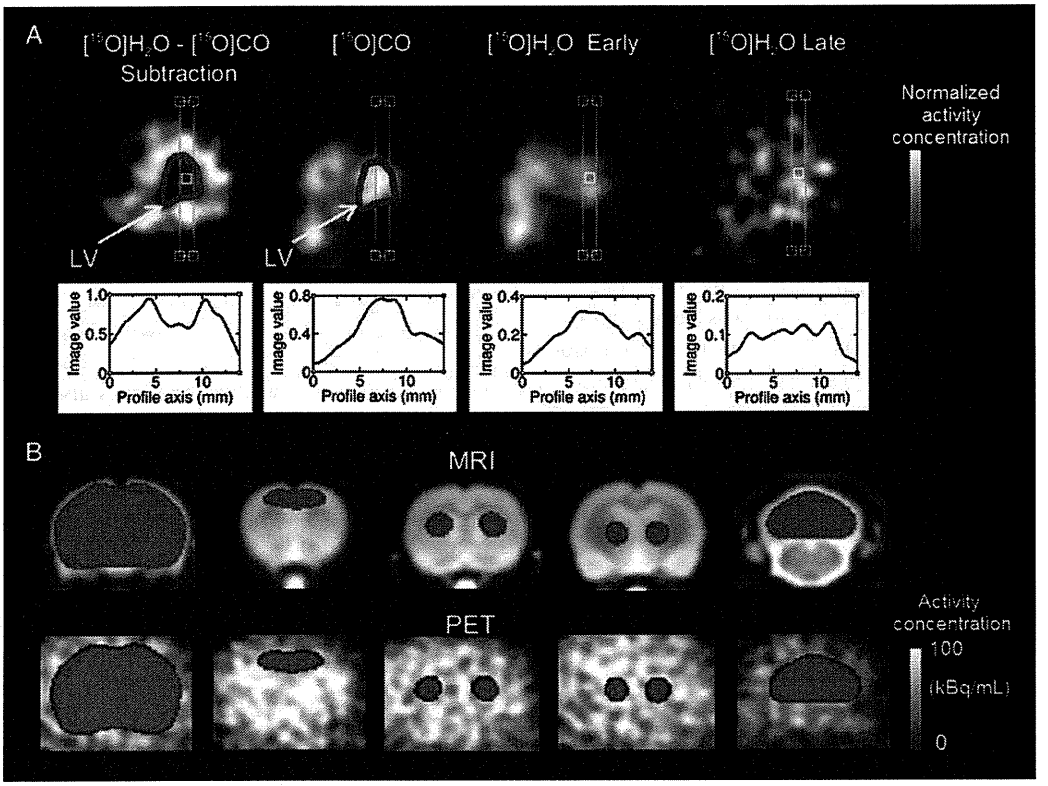

Fig. 3. VOIs. (A) VOI in the cardiac ventricle (delineated by red line). The VOI, delineated manually using the subtraction image of $[^{15}O]H_2O$ minus $[^{15}O]CO$ activity concentration (upper left), is transferred to the sum image of $[^{15}O]CO$ $[^{15}O]H_2O$ in the early phase (0–30 s) and $[^{15}O]H_2O$ in the late phase (150–180 s). Lower graphs show the profile of activity concentration on the line that is crossing the center of cardiac ventricle (as shown in light blue overlaid on the upper PET image). The image value in the graphs is in units of MBq/ml. Each PET image is shown in a gray color bar in an arbitrary range. (B) The coronal sections of MRI (upper) and PET images (lower) on which cerebral VOIs are overlaid in red. The furthest left section shows the whole-brain VOI. From the second left to right, the distance of each coronal slices was 2, 0, −2.6 and −12.0 mm from the bregma, each depicting the VOIs in the frontal cortex, striatum, thalamus and cerebellum, respectively. Each PET image was obtained by averaging dynamic PET images from 0 to 3 min. The activity concentration shown ranged from 0 to 100 kBq/ml as indicated in the gray color bar.

after normalization of the height and area under the curve. To eliminate variations in administered activity in each measurement, TACs were divided by the area under the curve (from 0 to 180 s). The rising time of each TAC was shifted to time zero by visual inspection. Then, the mean and standard deviation of the TACs were separately determined for each injection method and measurement modality. Finally, averaged TACs were normalized by their peak height and presented in the line chart (in Fig. 4A–B). A pair of AV-shunt and image-based TACs was obtained from the same PET measurement.

Since visual inspection of the shape of the average TAC led us to suspect significant dispersion in AV-shunt TAC as compared with image-based TAC, we investigated whether the dispersion could be corrected before calculating quantitative rCBF [9]. The correction of dispersion can be achieved by an empirical model of dispersion in which dispersion function was expressed in monoexponential function [9]. We estimated a dispersion time constant in this model equation using the "averaged TACs" of AV shunt and image based, since a statistical error in the TAC may affect the estimation of the dispersion. Dispersion time constants (τ) of 0, 5 and 10 s were used to derive deconvolved TACs from the mean AV-shunt TACs and were plotted against time along with the image-based mean TAC. Among three tested values for τ, we chose the optimal dispersion time constant for the AV-shunt TAC by visually inspecting consistency of the shape of TACs during the initial rising phase (faster: 0–15 s, slower: 0–30 s) between deconvoluted AV-shunt and the image-based TACs. We used a program for deconvolution written in the C programming language.

Then, we compared the "absolute" activity concentration of the TACs of the AV-shunt and image-derived techniques, both obtained simultaneously in the same animal and PET scan. This was primarily for the purpose of determining the adequacy of the calibration and confirming the suitability of the AV-shunt TAC using image-based TAC as a reference. As described previously, the activity concentration of the image-based TAC obtained from cardiac ventricle should reflect the sum of the underestimated activity concentration in the cardiac ventricle and spillover activity from surrounding tissues (cardiac wall tissues). Thus, we estimated the intraventricular blood activity concentration from imaged-

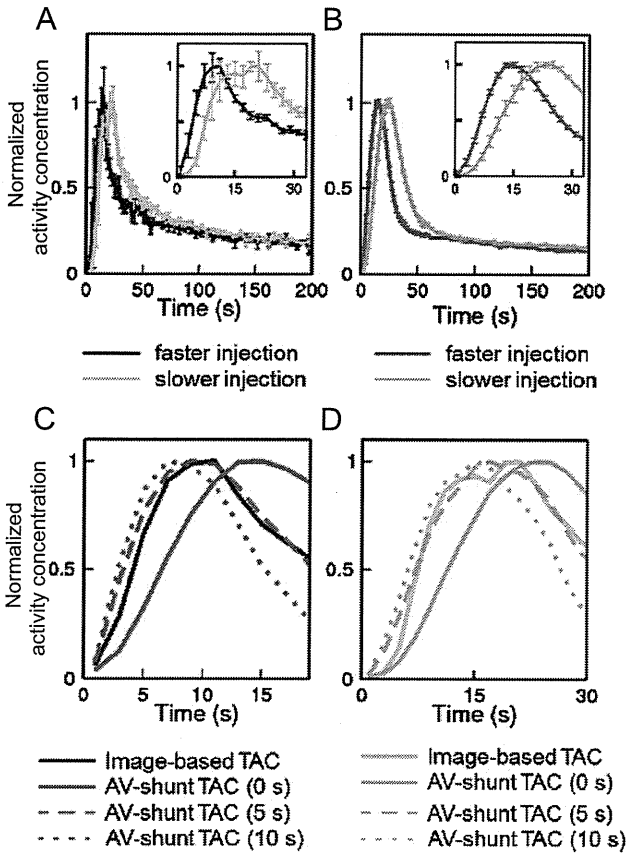

Fig. 4. Comparison of the normalized imaged-based and AV-shunt-derived TACs and of their dispersions. (A) Mean and standard deviation of normalized imaged-based TAC (obtained from the cardiac ventricular VOI) (n=3). Dark blue curve, faster injection; light blue curve, slower injection. (B) Mean and standard deviation of normalized AV shunt TAC (n=3). Red line, faster injection; orange line, slower injection. In each figure, the error bar indicates standard deviation, and the right upper inset shows the initial rising phase for a period of 30 s. Normalization was performed by scaling using the area under the curve and then the peak of TAC. Note that the standard deviation, particularly in the early rising phase, was much smaller in the AV-shunt TAC as compared with the image-based TAC. (C) Dispersion correction of AV-shunt TAC in faster injection. The blue line indicates the mean TAC obtained from the cardiac ventricle in the PET image, while red lines indicate the TAC of the AV shunt after correction of dispersion with time constants of 0, 5 and 10 s, respectively. (D) Dispersion correction of AV-shunt TAC in slower injection. The light blue line indicates the mean TAC obtained from the cardiac ventricle in the PET image, while orange lines indicate the TAC of the AV after correction of dispersion with time constants of 0, 5 and 10 s. In both faster and slower injection, the dispersion time constant of ~5 s appears to be the most optimal among the three for correcting the dispersion of AV-shunt TAC.

based TAC using a one-tissue, one-blood compartmental model of partial volume for the cardiac VOI [10]. The activity concentration in the cardiac ventricular VOI, $C_v(t)$ (Bq/ml), can be expressed by the following equation:

$$C_v(t) = \beta C_a(t) + \gamma \rho C_m(t), \quad (1)$$

where β is a recovery coefficient, γ is the spillover fraction of tissue activity concentration into left ventricle VOI, ρ is the density of myocardium (g/ml) and C_m the activity concentration of myocardium (Bq/g) [10]. Here, $\beta+\gamma=1$ if the heart (i.e., the dimensions of the left-ventricular cavity and myocardium) is "large" compared to the spatial resolution of the PET system [10]. The recovery coefficient (β) can be measured by calculating a ratio between mean activity concentration of the cardiac ventricular VOI during steady-state condition in the [^{15}O]CO scan (Fig. 3) and actual blood activity concentration sampled during that period, as described previously [11,12]. In addition, under an equilibrium state, the activity concentration of myocardium (C_m) can be estimated by the following equation:

$$C_m = pC_a, \quad (2)$$

where p is a partition coefficient of cardiac tissue (ml/g) and C_a is the activity concentration of [^{15}O]H_2O in blood (Bq/ml); thus, using Eqs. (1) and (2), C_a at an equilibrium state can be estimated from measured C_v by the following equation:

$$C_a = C_v/[\beta + (1-\beta)\rho p] \quad (3)$$

using known values of ρ and p, 1.04 g/ml and 0.91 ml/g, respectively [10]. Therefore, the comparison of the C_a values estimated from Eq. (3) with the activity concentration of AV shunt at steady state (this should correspond to the blood activity concentration) will mainly indicate the eligibility of the two techniques. Since the equilibrium was achieved at time t from 120 to 180 s after PET scan, the value of C_v was measured from the cardiac ventricular VOI by averaging the activity concentration of [^{15}O]H_2O during the corresponding period, and C_a was estimated from Eq. (3) using the measured value of β. The activity concentration of the AV shunt was obtained from averaged activity concentration during a period of 120–180 s and was compared with the values of C_a predicted from Eq. (3) and the image-based (cardiac ventricular VOI) TAC.

2.8. Regional CBF determination

Cerebral tissue TACs during [^{15}O]H_2O PET scans were obtained from five regions of interest in the brain: frontal cortex, striatum, thalamus, cerebellum and whole brain. A standard T2-weighted magnetic resonance image (MRI) of a rat [13] was automatically realigned to the summed PET image by means of an image registration tool in the FSL software (version 4.1.4) (http://www.fmrib.ox.ac.uk/fsl/index.html) [14]. The cross-modal image registration was performed using a cost function of mutual information. The VOI for each brain region was manually drawn on the standard MRI, realigned using an inverted transformation matrix to the PET image and used to obtain the TAC for each VOI (Fig. 3B). The VOI volumes were 1472, 44.0, 22.4, 13.5 and 106 mm^3 for the whole brain, frontal cortex, striatum, thalamus and cerebellum, respectively. The rCBF values were determined by using the input function of the

AV-shunt and cerebral TAC data in two steps. In the first step, we determined the time delay of the AV-shunt TAC as compared with cerebral whole-brain TAC by visual inspection. Using the predetermined time delay, the rCBF value for each region was estimated by means of a nonlinear least-square fitting procedure based on a one-tissue compartmental model [1–9,11–15], with unknown parameters of rCBF and partition coefficient p [16–18]. For the cerebral TAC, the initial period of 200 s was used for the fitting. The input function from the AV shunt was corrected for dispersion by deconvolving the original TAC using a single exponential function with a time constant of 5 s, determined based on the previous analysis.

Mathematical manipulations of TAC data and the fitting process to determine CBF were all performed using PyBLD (http://www.mi.med.osaka-u.ac.jp/pybld/pybld.html) built upon the Python language.

3. Results

3.1. Measurements of blood flow velocity in the AV-shunt line by ultrasonography

We evaluated the stability of the blood flow velocity in the AV-shunt line by comparing the relative velocity with that measured at a reference time point just before the [^{15}O] CO scan (Fig. 2). The time interval between the reference and the last time point (fourth) was 62±9 min. When scaled by the velocity at the reference point, the relative velocity at the later time ranged from 0.9 to 1.3 (Table 1), and there was no single case in which the flow velocity in the AV-shunt line was systematically biased during the experiments.

3.2. Comparisons of shape of TACs between different methods of injection and input measurement

Fig. 4A–B shows the average and the standard deviation of TACs in which the peak and area under the curve were normalized and averaged for each injection method (faster vs. slower) and measurement method (PET image based vs. AV shunt and GSO based). As predicted, the faster bolus injection showed an earlier rising time and a sharper initial phase of the TACs than after slower injection in both measurement methods. The image-based method provided a much faster and more rapid increase in the normalized activity and showed a sharper spike shape of the TAC, suggesting less dispersion of the curve shape. However, the standard deviation of the image-based TAC was relatively larger than that of the AV-shunt TAC, suggesting that the image-derived TACs suffer from more statistical noise and/or net detector sensitivity than the AV-shunt method. As also shown in Fig. 4, the AV-shunt-derived TACs were more dispersed than the image-derived converts, particularly in the initial portion of the curves, suggesting that a correction for the dispersion of AV-shunt-derived TACs may be required. The estimated time delays for the AV-shunt-derived versus the image-based TACs are listed in Table 2.

Table 1
Relative velocity of blood in the AV shunt during PET scan

	PET scan		
	Heart [^{15}O]CO	Heart [^{15}O]H_2O	Brain [^{15}O]H_2O
Relative velocity	1.0(0.1)	1.1 (0.1)	1.2 (0.1)

Values were scaled by the initial velocity measured before heart [^{15}O]CO PET scan. Number of observation was n=6 for each variable. Values were shown as mean (S.D.). The repeated-measure ANOVA did not show any significant effect of scans.

Table 2
Estimated time delay of AV-shunt TAC as compared with image-based TAC

Injection methods	Estimated delay (s)	
	Between AV-shunt TAC and image-based TAC of cardiac ventricle	Between AV-shunt TAC and whole-brain TAC
Faster injection	11 (9, 12)	9 (7, 11)
Slower injection	20 (18, 21)	17 (16, 18)

Values are shown in median (minimum, maximum) in unit of second. The number of observation was n=3 for each injection method. Two-way ANOVA with factors of injection speed (faster vs. slower) and reference TAC (image-based TAC vs. whole-brain TAC) disclosed significant effects of injection speed ($F_{1,8}$=89.7, P<.001) and reference TAC ($F_{1,8}$=5.82, P<.05).

3.3. Dispersion correction of AV-shunt TAC

Fig. 4C shows the effect of dispersion correction on averaged TACs. When corrected by τ=5 s, the shape of the dispersion-corrected mean AV-shunt TAC agreed well with that of the image-derived TAC, as compared with those with corrections of τ=0 and 10 s. We did not estimate the degree of dispersion for each single measurement since the deconvolution performed in the dispersion correction enhances the statistical noise of TAC curves, making it difficult to estimate the size of dispersion. Therefore, we applied the fixed value of τ=5 for correcting the dispersion for each AV-shunt TAC and used them for further analysis since the dispersion constant may be considered almost invariable if the geometry of blood flow paths including arterial architecture and AV-shunt line were the same across measurements.

3.4. Absolute activity concentration in the AV-shunt and image-derived TACs

Fig. 5A shows a comparison of the absolute activity concentration of the TACs obtained from the AV shunt and cardiac PET image in all the test animals. As shown in this figure, at the early phase, the peak of the AV-shunt TAC (red line) was higher than that of image-based TAC (blue line). As shown in Fig. 3A (in the panel second from the right), at the early phase of [^{15}O]H_2O scan, the activity concentration of the [^{15}O]H_2O was higher in the center of cardiac ventricle,

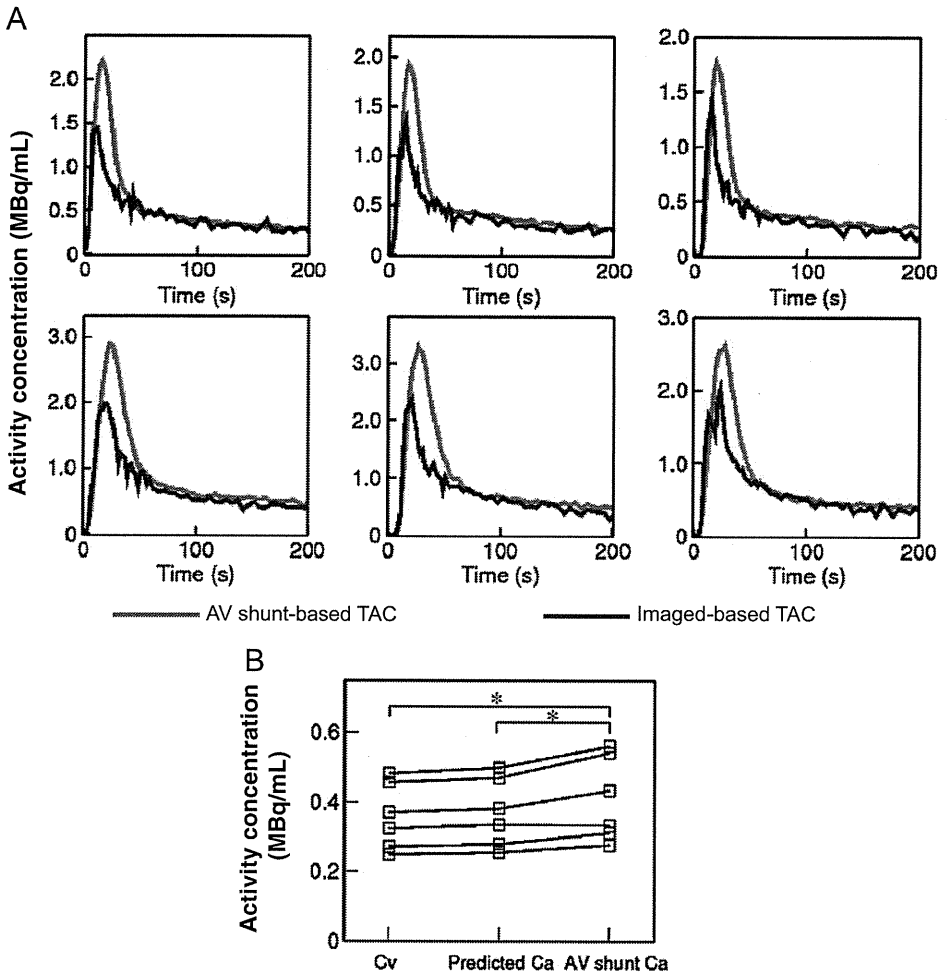

Fig. 5. Image-based and AV-shunt-derived TACs. (A) Absolute activity concentration of the AV-shunt TAC (red) and image-based cardiac ventricular TAC (blue) in all animals. The AV-shunt TAC (red) was corrected for dispersion (a time constant of 5 s), delay and calibration between the GSO detector and PET. Note that the image-based TAC shows almost comparable activity concentration as the AV shunt in the later equilibrium stage (from ~50 to 180 s), while it showed lower peak height of activity concentration in the early phase. (B) Activity concentration measured in the image-based cardiac ventricular VOI (C_v), predicted blood activity concentration (predicted C_a) and measured AV-shunt activity concentration (AV-shunt C_a). *P<.05 in paired t test.

suggesting the underestimation of blood activity concentration in the image-based TAC. Actually, the value of β (recovery coefficient for the cardiac VOI) was evaluated to be 0.43±0.05 from the data obtained during [^{15}O]CO scan (Table 3). The underestimation of the peak concentration was ~28.3%±4.4% by the image-based TAC as compared with AV-shunt TAC. In addition, at the later phase, the activity concentration of image-based TAC was comparable to the height of AV-shunt TAC in all animals (Fig. 5A),

Table 3
Measured and estimated variables from VOI of left ventricle

Variables	Mean±S.D.
VOI (μl)	29.0±0.3
Estimated recovery coefficient of left ventricular VOI (β)	0.43±0.05

Values were obtained from cardiac PET data with [^{15}O]CO and [^{15}O]H_2O (n=6).

suggesting that [^{15}O]H_2O diffused into the cardiac wall tissue and the spatial distribution of the activity extended over a larger region including the myocardial wall as well as the intraventricular cavity (i.e., a region whose dimensions were sufficiently large to minimize the partial volume effect). Consistent with this hypothesis, the count profiles over the late [^{15}O]H_2O images were flatter than those over the early images (Fig. 3A).

The foregoing was corroborated by comparison of the steady-state portions of the AV-shunt-derived TAC and of the imaged-derived curve based on the one-tissue, one-blood compartment model [Eq. (3)]. The averaged blood activity concentration (120<t<180 s) measured by the AV shunt varied from 0.28 to 0.56 MBq/ml (mean±S.D.=0.41±0.11 MBq/ml). The predicted blood activity from Eq. (3) using the image-based VOI data ranged from 0.25 to 0.50 kBq/ml (0.37±0.09 MBq/ml). Fig. 5B shows a plot of the measured image-based VOI activity concentration (C_v), blood activity

concentration predicted by Eq. (3) (predicted C_a) and AV-shunt blood activity concentration(AV-shunt C_a) in each animal. As shown in this figure, there was significant bias among three measures [repeated analysis of variance (ANOVA), $F_{2,\ 5}$=17.9, P<.001]. There was significant differences in blood activity concentration between C_v and AV-shunt C_a and between the predicted C_a and the AV-shunt C_a (post hoc pairwise comparison with correction multiple comparison, P<.05). There was a significant linear relationship between predicted C_a and AV-shunt C_a [AV-shunt C_a (MBq)=1.21∗predicted C_a (MBq)−4.0×10^{-2}, R^2=0.98, P<.001]. This suggests, however, that the bias was relatively small (i.e., only ~20%); the measured activity concentration of AV shunt at the steady state was comparable to and consistent with the blood activity concentration predicted from image-based VOI in the current system of rat heart/micro-PET.

3.5. Quantification of rCBF

The mean and S.D. of rCBF values (in ml/min/g) was 0.37±0.04 in the whole brain, 0.40±0.08 in the frontal cortex, 0.41±0.06 in the striatum, 0.36±0.04 in the thalamus and 0.36±0.05 in the cerebellum (see Table 4 for all the data). The mean and S.D. for partition coefficient (p) in the whole brain was 0.73±0.04 ml/g. No statistically significant difference was observed in rCBF values between faster and slower bolus injections (P>.05). Whole-brain rCBF values were plotted against pCO_2 values in all the animals except one, in which we failed to measure the pCO_2 (Fig. 6). As shown in this figure, a linear relationship was obtained between pCO_2 and whole-brain rCBF values [rCBF=0.01×pCO_2+0.06 (R^2=0.90, P<.001)]. The estimated time delay between whole-brain TAC and AV-shunt TAC is also listed in Table 2; as predicted, the estimated delay was consistently 3–4 s shorter than that between cardiac ventricular TAC and AV-shunt TAC for both injection methods.

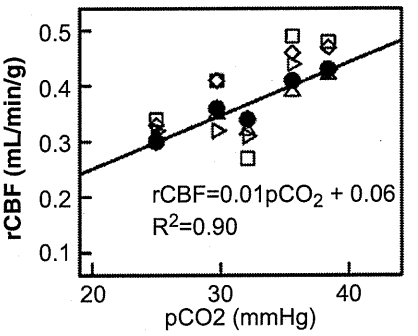

Fig. 6. Correlation between rCBF by brain region and blood pCO_2 using the AV-shunt-derived arterial input function. ●: whole brain, □: frontal cortex, ◇: striatum, Δ: thalamus, ▽: cerebellum.

4. Discussion

There has been no unbiased measurement method for arterial input function (as well as for blood flow) in rodents PET. The manual sampling may have been a conventional way of measuring input function, but apparently, it should have substantial bias due to insufficient temporal resolution. Invasiveness of this method makes it difficult for us to fully analyze or understand the actual bias of this system. In this paper, we described an AV-shunt technique for acquiring the arterial input function of [^{15}O]H_2O during PET acquisition in rats and used an image-based method as a reference of AV-shunt since it has already been used in the past literatures [2,10]. In the ultrasonographic evaluation of the blood flow through the AV shunt, none of the animals showed any evidence of stagnation in the shunt line, which potentially degrades the measurement of blood activity or the shape of AV-shunt TAC. The image-based TAC was obtained using the [^{15}O]H_2OPET data of the heart chamber based on a method described previously [10]. The results revealed that the count noise, one of the major error sources of activity concentration, was small in the AV-shunt TAC (as compared with image-based TAC) and that the shape of the AV-shunt-based TAC is not attenuated very much and could be properly corrected for time delay and dispersion. In contrast, the image-based method suffered from the partial volume effect even after the model-based correction, and the effect size was varied across time after injection. The PET scan for the brain with the AV shunt provided rCBF values that showed physiologically plausible variation depending on the blood carbon dioxide level. These findings suggest that the AV-shunt technique could be useful for future studies for rCBF measurements. The concept of the current study in

Table 4
rCBF values measured by [^{15}O]-H_2O PET and AV-shunt technique

Subjects	pCO_2	rCBF (p)				
		Whole brain	Frontal cortex	Striatum	Thalamus	Cerebellum
1	32.1	0.34 (0.77)	0.27 (0.64)	0.34 (0.86)	0.32 (0.94)	0.31 (0.76)
2	38.4	0.43 (0.80)	0.48 (0.88)	0.47 (0.89)	0.42 (0.86)	0.43 (0.78)
3	35.6	0.41 (0.71)	0.49 (0.80)	0.46 (0.79)	0.39 (0.96)	0.44 (0.72)
4	–	0.37 (0.70)	0.44 (0.77)	0.40 (0.79)	0.37 (0.77)	0.36 (0.66)
5	25.0	0.30 (0.69)	0.34 (0.71)	0.33 (0.73)	0.31 (0.74)	0.32 (0.72)
6	29.7	0.36 (0.69)	0.41 (0.73)	0.41 (0.78)	0.35 (0.80)	0.32 (0.65)

The values of pCO_2 are shown in unit of mmHg, rCBF in ml/g/min and p in ml/g, respectively. We failed to measure the value of pCO_2 of subject 4.

terms of bias and noise in measured arterial inputs is not new in the field of clinical nuclear medicine, but has been rarely taken into account in the field of molecular imaging in small animals. The results provide important messages for researchers who quantify CBF in rodents using PET.

One advantage of the AV-shunt TAC method over the image-based one may be higher temporal resolution and signal-to-noise ratio. As shown in Fig. 4, our approach for the AV-shunt-based TAC clearly detected different shapes of the input function between the faster and slower bolus injections, despite a small difference in the total period for injection. In addition, the figure shows that the error of the mean is also relatively smaller with the AV-shunt technique compared with the image-based one. These findings indicate that the AV-shunt-derived TAC may have less statistical error, mainly due to the high sensitivity of the detector geometry, and thus yield less propagated error associated with the calculated rCBF values than the image-based TAC. The shape of AV-shunt TAC may have been degraded by the dispersion; however, the amount of the dispersion was not too large ($\tau = 5$s), which was consistent for both injection methods (faster and slower) and was accurately correctable [19]. Iida et al. showed that, in humans, the arterial TAC derived from the radial artery was comparable to the cardiac image-derived TAC if the arterial TAC was corrected for dispersion using a time constant of 4 s [20]. In rats, Weber et al. estimated that the potential dispersion of TAC originating within the shunt tube was in a very small range, but they did not evaluate the actual dispersion time constant needed for correction. Thus, it is notable that our data show that the time constant of dispersion is small enough to properly correct dispersion of AV-shunt TAC in the current rat PET system.

Another notable advantage of the use of AV-shunt-based TAC over the image-based TAC is no necessity for correction of the height of the curve other than calibration for the activity concentration detectors. The activity concentration of cardiac ventricular VOI in the early phase of PET scan consistently showed lower values than those in the AV-shunt TAC, presumably due to predominant spill-out effect rather than spill-in in this early phase. Actually, the current data of [^{15}O]CO scan indicate that this underestimation was ~0.43 as a recovery coefficient (Table 3). The steady-state blood activity concentration estimated by AV shunt (AV-shunt C_a) was very close to that predicted from the image-based TAC.

Although we used imaged-based TAC as a reference, after correction for partial volume, it did not fully recover the blood activity concentration of [^{15}O]H_2O, particularly at the early phase of TAC. There was a significant underestimation in the initial phase (~28%) and even in the steady-state period (~20%) (Fig. 5A). The reason for this underestimation may be due to the small size of the heart as compared with the resolution of the current PET scanner, which violates the assumption of the model equation for partial volume (i.e., $\beta+\gamma=1$). Actually, our [^{15}O]CO results showed small value of recovery coefficient (~0.43) for the left-ventricle ROI, and previous simulation studies also indicated that recovery coefficient of less than 0.65 may result in underestimation of TAC when derived from human left ventricle [10]. Thus, future studies should improve the model to obtain accurate blood TAC from PET image in rat heart.

Other investigators have attempted to derive to a standard input function for small-animal PET study but for a more slowly cleared and localizing tracer, namely, ^{18}F-fluorodeoxyglucose [21]. Because of the fast kinetics of [^{15}O]H_2O, it may be difficult to use the standard input function for this tracer; thus, it requires to be evaluated in detail. In particular, the difference in the delay time of the rising time of TAC should be strictly standardized. In addition, the injection rate of tracer activity concentration should always be standardized, so that an automatic injector that allows a constant infusion of the tracer is recommended. Further, our results suggest that, with careful standardized injections, the use of average small-animal arterial input functions for "fast" tracers such as [^{15}O]H_2O as well as "slower" tracers such as [123I]iodoamphetamine may be valid.

Our motivation to measure blood flow velocity in the AV shunt by ultrasonography was concern for potential occlusion of the line by blood clotting during experiments, which may affect the shape of arterial input curves. Weber et al. showed that there were rare cases of clogging in their AV-shunt method where they did not perform heparinization beforehand and used multiple stopcocks for blood sampling, which may have induced turbulent blood flow and facilitated clot formation [5]. In our case, the AV-shunt line and the animals' blood were both heparinized, and no three-way stopcock was used in the AV-shunt line, thereby avoiding any potential clot inducing of blood flow. The flow velocity inside the tube did not actually decrease within a period of about 1 h during the experiments, suggesting that clot formation was successfully prevented by the current method. On the other hand, there may be potential bleeding when heparin is administered, but none of the test animals in the current study showed such bleeding during the experiments.

There is an extensive literature on the relationship between rCBF and pCO_2. Our study showed a significant correlation between rCBF and pCO_2; in particular, the slope of the regression line ($\Delta CBF/\Delta pCO_2$=0.01) was comparable to that obtained in primate animals by Grubb et al. [22]. By an intracarotid injection method using [^{15}O]H_2O tracer and [^{15}O]CO, they showed that the rCBF values of anesthetized monkeys had the following relationship with pCO_2: rCBF (ml/g/min)=0.018×pCO_2 (mmHg)−0.17. Other researchers also reported that, in anesthetized monkeys, the value of $\Delta CBF/\Delta pCO_2$ was 0.011 [23] and 0.012 [24]. In recent literature, Williams et al. (1992) reported that rCBF measured by a spin-labeling method using MRI had a linear relationship with arterial pCO_2 in anesthetized rats and that the value of $\Delta CBF/\Delta pCO_2$ was 0.052 [25]. Despite variations in species, anesthetic conditions and measurement methods, our data demonstrating the linear relationship

between rCBF and pCO_2 in rats are consistent with these previous studies.

Our study has several implications for future research in neurophysiology. First, the current method could be used for repeated measurements of quantitative CBF in a single experiment. This could be useful, for example, to evaluate acute hemodynamic changes after pharmacological intervention or during behavioral tasks. It also allows measurement of the cerebral metabolic rate of oxygen utilization, which requires different PET scans using multiple tracers, such as ^{15}O-labeled water, oxygen and carbon monoxide [26]. Second, the current AV-shunt method could be used for other radiotracers not only for PET but also for single photon emission computed tomography since the GSO detector we used is sensitive to a wide range of photon energies [7]. Third, the current AV-shunt technique can be used in the future to validate more empirical methods of image-based TAC derivation (e.g., Yee et al. [2]) under various possible conditions.

There are several limitations in the AV-shunt technique. First, this method may be technically demanding and particularly difficult when measuring very frequently on different days in the same animal. The catheterized femoral artery and vein were sutured and occluded after the experiment; thus, it is difficult to repeat this study more than twice in the same animal. This could be overcome by using microsurgery to suture the arterial walls without occluding the lumen. Second, the estimation of dispersion may be difficult in each measurement due to the statistical noise in the measured TAC. Therefore, preparation of the AV shunt must be performed in the same manner, particularly in terms of the length and caliber of the shunt tube, site of artery catheter placement and physiological conditions of the animals, which may affect the laminar flow of sampling blood.

5. Conclusions

We confirmed the stability of the AV-shunt technique for measurement of the arterial input function in small animals. The AV-shunt method allowed us to obtain input TAC with less statistical noise than the image-based one and to calculate rCBF using the micro-PET scanner, and proved to be quantitative in identifying physiological changes in rCBF. In contrast, the image-based TAC suffered from the partial volume and could not be fully recovered even after correction particularly during the initial peak phase of input TAC of $[^{15}O]H_2O$. The AV-shunt technique could be useful for less invasive measurement of cerebral hemodynamics in small animals than the conventional blood sampling method.

Acknowledgments

This study was supported by a grant of KAKENHI from the Ministry of Education, Culture, Sports, Science and Technology (MEXT), Japan, and a grant from the National Institute of Biomedical Innovation, Saito, Japan.

References

[1] Kanno I, Iida H, Miura S, Murakami M, Takahashi K, Sasaki H, et al. A system for cerebral blood flow measurement using an $H_2^{15}O$ autoradiographic method and positron emission tomography. J Cereb Blood Flow Metab 1987;7:143–53.

[2] Yee S, Jerabek PA, Fox PT. Non-invasive quantification of cerebral blood flow for rats by microPET imaging of ^{15}O labelled water: the application of a cardiac time-activity curve for the tracer arterial input function. Nucl Med Commun 2005;26:903–11.

[3] Matsumoto A, Namon R, Utsunomiya Y, Kogure K, Scheinberg P, Reinmuth OM. The measurement of cerebral blood flow in the rat. Stroke 1975;6:630–7.

[4] Ingvar M, Eriksson L, Rogers GA, Stone-Elander S, Widén L. Rapid feasibility studies of tracers for positron emission tomography: high-resolution PET in small animals with kinetic analysis. J Cereb Blood Flow Metab 1991;11:926–31.

[5] Weber B, Burger C, Biro P, Buck A. A femoral arteriovenous shunt facilitates arterial whole blood sampling in animals. Eur J Nucl Med Mol Imaging 2002;29:319–23.

[6] Weber B, Späth N, Wyss M, Wild D, Burger C, Stanley R, et al. Quantitative cerebral blood flow measurements in the rat using a beta-probe and $H_2^{15}O$. J Cereb Blood Flow Metab 2003;23:1455–60.

[7] Kudomi N, Eunjoo C, Yamamoto S, Watabe H, Kyeong, Min K, et al. Development of a GSO detector assembly for a continuous blood sampling system. EEE Trans NuclSci 2003;50:70–3.

[8] Kim JS, Lee JS, Im KC, Kim SJ, Kim S, Lee DS, et al. Performance measurement of the microPET focus 120 scanner. J Nucl Med 2007; 48:1527–35.

[9] Iida H, Kanno I, Miura S, Murakami M, Takahashi K, Uemura K. Error analysis of a quantitative cerebral blood flow measurement using $H_2^{15}O$ autoradiography and positron emission tomography, with respect to the dispersion of the input function. J Cereb Blood Flow Metab 1986; 6:536–45.

[10] Iida H, Rhodes CG, de Silva R, Araujo LI, Bloomfield PM, Lammertsma AA, et al. Use of the left ventricular time-activity curve as a noninvasive input function in dynamic oxygen-15-water positron emission tomography. J Nucl Med 1992;33(9):1669–77.

[11] Bergmann SR, Fox KA, Rand AL, McElvany KD, Welch MJ, Markham J, et al. Quantification of regional myocardial blood flow in vivo with $H_2^{15}O$. Circulation 1984;70:724–33.

[12] Araujo LI, Lammertsma AA, Rhodes CG, McFalls EO, Iida H, Rechavia E, et al. Noninvasive quantification of regional myocardial blood flow in coronary artery disease with oxygen-15-labeled carbon dioxide inhalation and positron emission tomography. Circulation 1991;83:875–85.

[13] Schweinhardt P, Fransson P, Olson L, Spenger C, Andersson JLR. A template for spatial normalisation of MR images of the rat brain. J Neurosci Methods 2003;129(2):105–13.

[14] Smith SM, Jenkinson M, Woolrich MW, Beckmann CF, Behrens TEJ, Johansen-Berg H, et al. Advances in functional and structural MR image analysis and implementation as FSL. Neuroimage 23 Suppl 2004;1:S208–19.

[15] Kety SS, Schmidt CF. The nitrous oxide method for the quantitative determination of cerebral blood flow in man; theory, procedure and normal values. J Clin Invest 1948;27:476–83.

[16] Huang SC, Carson RE, Hoffman EJ, Carson J, MacDonald N, Barrio JR, et al. Quantitative measurement of local cerebral blood flow in humans by positron computed tomography and ^{15}O-water. J Cereb Blood Flow Metab 1983;3:141–53.

[17] Iida H, Kanno I, Miura S, Murakami M, Takahashi K, Uemura K. A determination of the regional brain/blood partition coefficient of water

using dynamic positron emission tomography. J Cereb Blood Flow Metab 1989;9:874–85.

[18] Magata Y, Temma T, Iida H, Ogawa M, Mukai T, Iida Y, et al. Development of injectable O-15 oxygen and estimation of rat OEF. J Cereb Blood Flow Metab 2003;23:671–6.

[19] Iida H, Kanno I, Miura S, Murakami M, Takahashi K, Uemura K. Error analysis of a quantitative cerebral blood flow measurement using $H_2^{15}O$ autoradiography and positron emission tomography, with respect to the dispersion of the input function. J Cereb Blood Flow Metab 1986;6(5):536–45.

[20] Iida H, Miura S, Shoji Y, Ogawa T, Kado H, Narita Y, et al. Noninvasive quantitation of cerebral blood flow using oxygen-15-water and a dual-PET system. J Nucl Med 1998;39(10):1789–98.

[21] Meyer PT, Circiumaru V, Cardi CA, Thomas DH, Bal H, Acton PD. Simplified quantification of small animal [^{18}F]FDG PET studies using a standard arterial input function. Eur J Nucl Med Mol Imaging 2006;33:948–54.

[22] Grubb RL, Raichle ME, Eichling JO, Ter-Pogossian MM. The effects of changes in $PaCO_2$ on cerebral blood volume, blood flow, and vascular mean transit time. Stroke 1974;5:630–9.

[23] White JC, Brooks JR, Goldthwait JC, Adams RD. Changes in brain volume and blood content after experimental concussion. Ann Surg 1943;118(4):619–33.

[24] James IM, Millar RA, Purves MJ. Observations on the extrinsic neural control of cerebral blood flow in the baboon. Circ Res 1969;25(1):77–93.

[25] Williams DS, Detre JA, Leigh JS, Koretsky AP. Magnetic resonance imaging of perfusion using spin inversion of arterial water. Proc Natl Acad Sci USA 1992;89:212–6.

[26] Kudomi N, Hayashi T, Teramoto N, Watabe H, Kawachi N, Ohta Y, et al. Rapid quantitative measurement of CMRO2 and CBF by dual administration of 15O-labeled oxygen and water during a single PET scan-a validation study and error analysis in anesthetized monkeys. J Cereb Blood Flow Metab 2005;25(9):1209–24.

Biomaterials 33 (2012) 2439–2448

Contents lists available at SciVerse ScienceDirect

Biomaterials

journal homepage: www.elsevier.com/locate/biomaterials

The use of magnetic resonance cell tracking to monitor endothelial progenitor cells in a rat hindlimb ischemic model

Carlos A. Agudelo [a], Yoichi Tachibana [b], Andres F. Hurtado [a], Takayuki Ose [b], Hidehiro Iida [b], Tetsuji Yamaoka [a,*]

[a] Department of Biomedical Engineering, National Cardiovascular Center Research Institute, 5-7-1 Fujishiro-dai, Suita, Osaka 565-8565, Japan
[b] Department of Investigative Radiology Advanced Medical Engineering Center, National Cerebral and Cardiovascular Center Research Institute, 5-7-1 Fujishiro-dai, Suita, Osaka 565-8565, Japan

ARTICLE INFO

Article history:
Received 7 November 2011
Accepted 25 November 2011
Available online 27 December 2011

Keywords:
Dextran
MRI
Progenitor cell
Transplantation

ABSTRACT

A water-soluble magnetic resonance imaging (MRI) contrast agent, Dextran mono-N-succinimidyl 1,4,7,10-tetraazacyclododecane-1,4,7,10-tetraacetate-gadolinium^{3+} (Dex-DOTA-Gd^{3+}), was shown to enable monitoring of the anatomical migration and the survival period of transplanted stem cells for up to 1 month. Gadolinium molecules in the cells were rapidly eliminated from the site and excreted upon cell death. Endothelial progenitor cells (EPCs) transplanted into the inguinal femoral muscle of rats migrated distally through the knee in rats after hindlimb ischemia but did not migrate in non-ischemic rats. Interestingly, the survival period of transplanted EPCs was notably prolonged in the ischemic limb, indicating that EPCs are required by the ischemic tissues and that the fate of transplanted EPCs was affected by the disease. Compared to the commonly used particle type of MRI contrast agents, the system described in this study is expected to be invaluable to help clarifying the process of stem cell transplantation therapy.

1. Introduction

In the last decades, transplantation of hematopoietic stem cells, bone marrow (BM)-derived mesenchymal stem cells, and adipose tissue-derived mesenchymal stem cells has been reported to stimulate regeneration of different tissues such as ischemic limb [1–6], ischemic myocardium [7–9], and brain [10]. Endothelial progenitor cells (EPCs), which are crucial in the regeneration of injured tissues and organs, act through a molecular mechanism known as angiogenesis [10,11]. This post-natal revascularization starts with the recruitment of EPCs from stem cell reservoirs such as BM [12,13]. According to the paradigm of angiogenesis, EPC transplantation may offer a source of feasible endothelial cells that migrate and proliferate from preexisting blood vessels, thus promoting revascularization in the ischemic limb, contributing to angiogenesis [10,14]. Although the mechanisms of homing and differentiation of EPCs are not well understood, tissue ischemia results in the upregulation of several angiogenic factors such as vascular endothelial growth factor (VEGF), which interacts with 2 tyrosine kinase receptors, VEGF receptor-2 (VEGF-R2 or fetal liver kinase 1 [Flk-1], kinase domain receptor [KDR]) and VEGF receptor-1 (VEGFR1, Flt-1), stromal cell-derived factor-1 (SDF-1), insulin-like growth factor-1 (IGF-1), and hepatocyte growth factor (HGF). These growth factors are all expressed in several cell types, including EPCs, that promote migration to the injury site [15,19]. However, some studies have shown that neovascularization of ischemic tissues may not be exclusively attributed to the incorporation of EPCs into the vessels, but also to paracrine effects that probably influence the process of angiogenesis by releasing pro-angiogenic factors [20,21].

The ability to noninvasively track cells in vivo and follow their location after transplantation would significantly contribute to our understanding of the effects of stem cell therapy. Magnetic resonance imaging (MRI) is one of the noninvasive methods employed to examine the migratory behavior of stem and progenitor cells based on its whole-body spatial resolution, even in three-dimensional images. In MRI cell tracking, contrast agents are used to improve the quality of an image or to label transplanted cells to facilitate the detection of their location within the tissue. The most commonly used contrast agents, which have been successfully employed in tracking a variety of cell lineages, are superparamagnetic iron oxide (SPIO) and its derivatives. Progenitor cells have been tracked in vitro by using Tat peptide-derived SPIO. The high contrast of SPIO-labeled cells allows imaging of a single cell [22]. Other studies have demonstrated the feasibility of imaging

* Corresponding author. Fax: +81 6 6835 5476.
E-mail address: yamtet@ri.ncvc.go.jp (T. Yamaoka).

0142-9612/$ – see front matter © 2011 Elsevier Ltd. All rights reserved.
doi:10.1016/j.biomaterials.2011.11.075

small quantities of SPIO-labeled cells using high-resolution MRI [23,24]. Bulte et al. reported in vivo tracking of migrating cells labeled with dextran-coated iron oxide in the brain parenchyma for about 32 days [24]. Long-term monitoring of SPIO-labeled cells has also been reported by Guzman et al. in transplanted human neural stem cells [25] and Hoehn et al. in embryonic stem cells [26].

Despite the high sensitivity and resolution of SPIO tracking of labeled stem cells in vivo, this method has some disadvantages. In one report, the MRI signal that was attributed to the transplanted stem cells was found to actually be produced by macrophages that had phagocytosed the iron particles. When tracking mesenchymal stem cells in infarcted myocardium, Amsalem et al. reported that the signal was generated by cardiac macrophages that engulfed SPIO [27]. This phenomenon was lately confirmed by Terrovitis et al., who also demonstrated that the MRI signal was generated by iron-loaded macrophages rather than iron-labeled stem cells [28].

In another study by Li et al. [29] tracking human embryonic stem cells and endothelial cells by using iron particles and reporter gene for tracking implanted cells into hind limbs, showed a discrepancy between the acquired MRI signal of cells, which persisted for 28 days post-transplantation, and the genetically introduced bioluminescent signal that progressively decreased within 2 weeks. Further histological analysis revealed that most of the iron particles were taken up by macrophages in the ischemic limb. In a recent report, Winter et al. demonstrated that iron oxide fails to distinguish dead from living transplanted cells in non-obese diabetic/severe combined immunodeficient mice [30].

These reports indicate that although this method is useful for tracking the anatomic location of labeled cells after direct implantation, it does not provide reliable information about cell fate in the long term.

We previously developed water-soluble polymeric gadolinium chelate contrast agents for labeling NIH-3T3 cells [31]. Since, water-soluble polymers behave very differently from the particulate materials [32,33], the problems with the SPIO was expected to be solved. We then recently selected dextrans (Dex) as biocompatible carriers [34] and succeeded to label BM-derived EPCs with Dextran-mono-N-succinimidyl 1,4,7,10-tetraazacyclododecane-1,4,7,10-tetraacetate-gadolinium^{3+} (Dex-DOTA-Gd^{3+}). Dex-DOTA-Gd^{3+} demonstrated the excellent capacity for ex vivo cell labeling before transplantation, a high intracellular stability, and biocompatibility without affecting cell viability and proliferation [35].

EPC transplantation therapy is of remarkable importance in the regeneration process of ischemic tissues. Therefore, there is a critical need to refine the techniques for visualization of EPC recruitment, homing, and migration that accompany the release of various cytokines, which is a process that needs to be studied more carefully.

If we hypothesize that living EPCs labeled with Dex-DOTA-Gd^{3+} can be tracked by MRI during their migration from the transplantation point to the foci of vascularization, the behavioral pattern of these cells in an ischemic limb should differ from that in a non-ischemic limb and also from the pattern exhibited by SPIO-labeled cells. We also challenged the quantification of cell survival by measuring the amount of excreted Gd on the basis of the feature of the contrast agent that will be probably released from dead cells and rapidly cleared from the body.

2. Materials and methods

2.1. Isolation of EPCs

All animal experiments were performed according to a protocol approved by our animal facility and use committee. BM was flushed from femurs and tibias of F344 rats (4 weeks old, male) after previous cytokine-induced mobilization of BM-derived EPCs by using granulocyte colony-stimulating factor (G-CSF, Kirin Pharma, Japan) (200 μg kg^{-1}·day^{-1} for 5 days, subcutaneously injected) [36]. CD34- and Flk-1-positive BM cells were isolated using magnetic beads (Streptavidin Microbeads, Miltenyi Biotec GmbH, Gladbach, Germany) coated with anti CD34 and Flk-1 antibodies (sc-6251 and sc-7324, Santa Cruz Biotechnology Inc., CA) and a Biotin Labeling kit-NH_2 (Dojindo Molecular Technologies Inc., Japan). Cells were placed in fibronectin-coated dishes and cultured with an endothelial cell basal medium (EBM-2) supplemented with endothelial growth medium 2 (EGM-2 SingleQuots, Clonetics Lonza, Walkersville, MD) [15].

2.2. Rat ischemic limb model

To investigate if Dex-DOTA-Gd^{3+} labeling may have any adverse effect on the neovascularization of a rat ischemic limb model, male F344 rats (8 weeks old) were anesthetized with isoflurane (1.5% in air). The left femoral artery and vein and their branches were ligated and completely excised through a skin incision [37]. Rats ($n = 6$) were injected in 3 places with a total of 150 μl of Bolheal® containing Dex-DOTA-Gd^{+3}-labeled EPCs [35]. Injections were applied as follows: to allow normal movement of the cells through the muscle, 6.3×10^6 labeled cells in 75 μl Bolheal® component A (thrombin, 250 unit/ml) were intramuscularly injected in 3 different places in the abductor and quadriceps (total $1.8–2 \times 10^7$ cells) and then, 75 μl Bolheal® component B (fibrinogen, 80 mg/ml) was injected in the same sites to temporarily immobilize the cells (gelation occurred in the muscle). Ischemic limb controls ($n = 6$) were injected with Bolheal® which did not contain cells.

2.3. Laser Doppler analysis

The ratio of the ischemic (left)/non-ischemic (right) limb blood flow was measured by using a Laser Doppler Perfusion Imager (LDPI; Moor Instruments Ltd., MoorLDI, Millwey, England). Blood flow was scanned twice and images were subjected to computer-assisted quantification. The average blood flow of ischemic and non-ischemic limbs was calculated.

2.4. Angiography

Angiograms were obtained 35 days after transplantation of Dex-DOTA-Gd^{3+}-labeled EPCs. Animals were anesthetized and a pig tail catheter was positioned in the distal abdominal aorta approximately 1.5 cm above the iliac bifurcation, and anteroposterior digital subtraction angiograms of the pelvis and both limbs were acquired at a film rate of 15 frames per second using a digital mobile imaging system (GE OEC 9800 system, GE OEC Salt Lake City, UT) (control rats: $n = 3$, EPC-transplanted rats: $n = 3$). Omnipaque-350 (iohexol) was injected at rate of 400 μl/s (total: 1.2 ml) [6].

2.5. MRI measurements

Dex-DOTA-Gd^{3+}-labeled EPCs were identified in vivo using T1-weighted images obtained with a 1.5-T compact MRI system (MRmini, Dainippon Sumitomo Pharma, Osaka, Japan) with a repetition time (TR) of 2000 ms and an echo time (TE) of 9 ms (field of view [FOV], 4 × 8 cm; matrix, 126 × 256; slice thickness, 1 mm; slice gap, 0 mm; number of slices, 35).

2.6. Gadolinium concentration in cells, organs, urine, and feces

To quantify the concentration of Gd(III) paramagnetic species in labeled EPCs, cells were placed in 60-mm dishes and cultured for 1 day. EPCs were electroporated as described in supplementary methods and then, detached, counted, and placed in 15-ml tubes. Samples were treated with nitric acid to measure the concentration of Gd by inductively coupled plasma atomic emission spectroscopy (ICP-AES, Model 8500, Shimadzu Co., Kyoto, Japan).

2.7. Statistical analysis

All data are expressed as means ± SD. Statistical significance was evaluated using an unpaired 2-tailed Student's *t test* for 2 variables. Differences were considered significant when P values were less than 0.05.

3. Results

3.1. Dex-DOTA-Gd^{3+}-labeled EPCs

BM-derived cells (passage 4-5) that incorporated lectin and DiI-acLDL are shown in Supplementary Fig. 1A–D, respectively. Double-positive cells (Supplementary Fig. 1E and F) were identified as EPCs [15,18,19]. Additional staining with eNOS was performed (Santa Cruz Biotechnology Inc., Santa Cruz, CA, 20 μg/ml, $n = 3$) at 37 °C for 4 h. BM-derived cells that were stained positive

for eNOS where confirmed to exhibit an endothelial phenotype [37,15].

The Impact of Dex-DOTA-Gd^{3+} labeling on the expression of four membrane proteins specific to the endothelial phenotype (Fig. 1E). In the same culture condition, tree different samples were analyzed on days 1 and 2 after labeling by electroporation. PECAM-1 platelet endothelial cell adhesion molecule 1 (CD31), VE-cadherin (CD144), and CD34 expression were unchanged on day 1, but slightly rose on day 2. However these increased was non-statistically significant. The expression CD29, which represents mesenchymal stem cells, was stable on day 1 and 2.

After synthesis [35], EPCs were labeled by electroporation with the contrast agent Dex-DOTA-Gd^{3+}, whose structure is shown in Fig. 1A. Labeled EPCs showed bright fluorescence in the cytoplasm under the confocal scanning microscope, reflecting the presence of large amounts of contrast agent (Fig. 1B). Interestingly, magnified images of labeled cells (Fig. 1C) revealed that no further transport into the nucleus was observed 25 days after labeling.

It is well known that EPCs induce neovascularization by incorporating cells into formed vessels and releasing angiogenic factors in a paracrine manner [20,21]. We then examined the effect of Dex-DOTA-Gd^{3+} labeling on the expression of pro-angiogenic factors specific to EPCs such as VEGF, HGF, SDF-1, and IGF1. The expression of growth factors related to GAPDH in EPCs was not statistically different compared to Dex-DOTA-Gd^{3+}-labeled cells 2 days after electroporation ($P > 0.05$) (Fig. 1D).

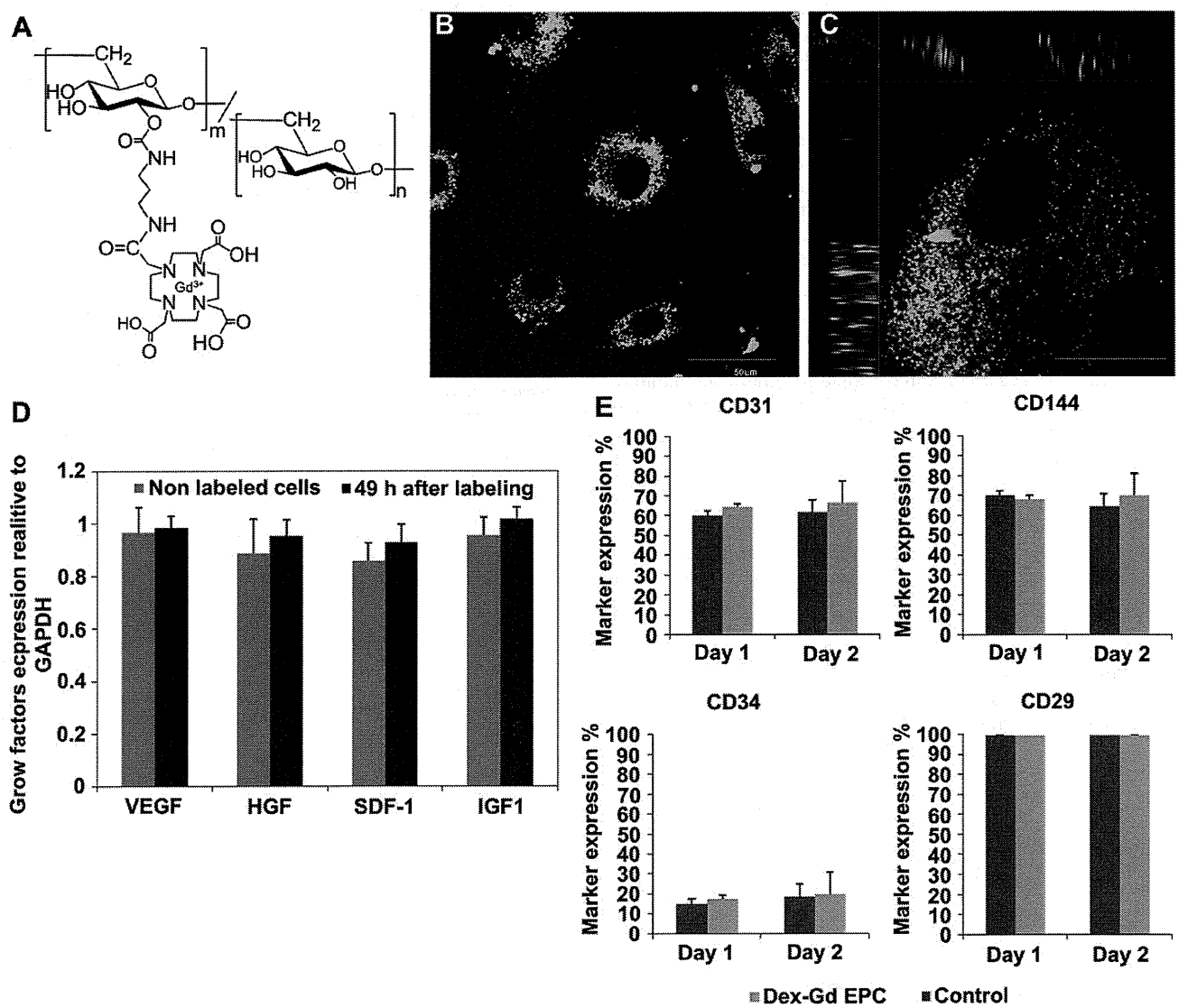

Fig. 1. Dextran-mono-N-succinimidyl 1,4,7,10-tetraazacyclododecane-1,4,7,10-tetraacetate-gadolinium^{3+} (Dex-DOTA-Gd^{3+}) as an magnetic resonance imaging (MRI) contrast agent. (A) Chemical structure of Dex-DOTA-$Gd.^{3+}$(B–C) Confocal microscopy of Dex-DOTA-Gd^{3+}-labeled endothelial progenitor cells (EPCs) after electroporation. Scale bar = 50 μm (left) and 25 μm (right). (D) Cellular expression levels of pro-angiogenic growth factors such as vascular endothelial growth factor (VEGF), hepatocyte growth factor (HGF), stromal cell-derived factor-1 (SDF-1), and insulin-like growth factor-1 (IGF-1) in Dex-DOTA-Gd^{3+}-labeled EPCs 48 h after electroporation. The mean (±SD) values of cellular expression relative to glyceraldehyde-3-phosphate dehydrogenase (GAPDH) are shown; no statistically significant differences were identified between labeled and unlabeled EPCs ($n = 6$) *$P > 0.05$. (E) EPC membrane marker expression. Percentage of the marker expression by FACS was performed in 4 different markers: CD31, CD144, CD34, and CD29, at days 1 and 2 after Dex-DOTA-Gd^{3+} labeling by electroporation. No significant changes in expression markers were observed on both days, compared to unlabeled EPC (control). FACS analysis was performed in triplicate, with three different samples, for all markers. Bars represent the standard deviation between different samples. No statistically significant differences were identified between labeled and unlabeled EPCs.

3.2. Effect of Dex-DOTA-Gd^{3+} on ischemic limb healing

We evaluated whether Dex-DOTA-Gd^{3+} as a contrast agent has an adverse effect on the capacity of EPCs to promote angiogenesis and neovascularization of ischemic limbs. Subcutaneous blood flow perfusion was analyzed using an LDPI (Fig. 2A). The ischemic limb blood perfusion ratios in animals implanted with Dex-DOTA-Gd^{3+}-labeled EPCs showed that blood perfusion increased after 5 days (red to white color distribution, 54% increase at day 30, $P < 0.001$) compared with control rats, in which an increase in blood perfusion was barely detected (Fig. 2B). On the basis of the results of the blood perfusion analysis, conventional angiograms were obtained 35 days after Dex-DOTA-Gd^{3+}-labeled EPCs were implanted in ischemic limbs. Microangiography allowed the visualization of the arterial network of an ischemic limb after transplantation of Dex-DOTA-Gd^{3+}-labeled EPCs and showed an increase in the number of small arteries after excision of the femoral artery and vein (Fig. 2D) [38]. Most of them originated from the trunk of the iliac artery. This gathering feature of the arteries was not observed in the branching pattern of control ischemic arteries (Fig. 2C). Angiography confirmed that Dex-DOTA-Gd^{3+}-labeled EPCs are capable of promoting the formation of collateral vessels in ischemic limbs.

Supplementary video related to this article can be found at doi: 10.1016/j.biomaterials.2011.11.075.

3.3. EPC migration in ischemic and non-ischemic limbs

Having demonstrated that MRI of EPCs by means of Dex-DOTA-Gd^{3+} did not affect the ability of EPCs to regenerate injured tissues, we tested the hypothesis that the behavioral pattern of these cells in an ischemic limb should differ from that in a non-ischemic limb and also from the pattern exhibited by SPIO-labeled cells, by using a different group of F344 rats (male, 8 weeks old $n = 3$). Rats were implanted with 1×10^7 labeled cells to analyze the pattern of migration exhibited by Dex-DOTA-Gd^{3+}-labeled EPCs in non-ischemic and ischemic limb models, as well in SPIO-labeled EPCs in ischemic models. The position of the animals in the MRI machine is indicated in Fig. 4A and was considered more adequate to understand the fate and migration of labeled EPCs. T1-weighted images of the rats were acquired with 2D and 3D spin-echo sequences at a TR of 2000 ms, a TE of 12 ms, coronal slice thickness of 1 mm, average 2, and image acquisition matrix of 128×256. Dex-DOTA-Gd^{3+} labeled EPCs transplanted into the ischemic limb were visualized within 14 days after transplantation. Cells were observed in the adductor and quadriceps, and migration in the direction of the knee muscle was as indicated by arrows in Supplementary Fig. 2. Labeled cells were completely banished after 14 days. To elucidate the spatial location and biodistribution of transplanted labeled cells, the acquired MRIs were modeled by the

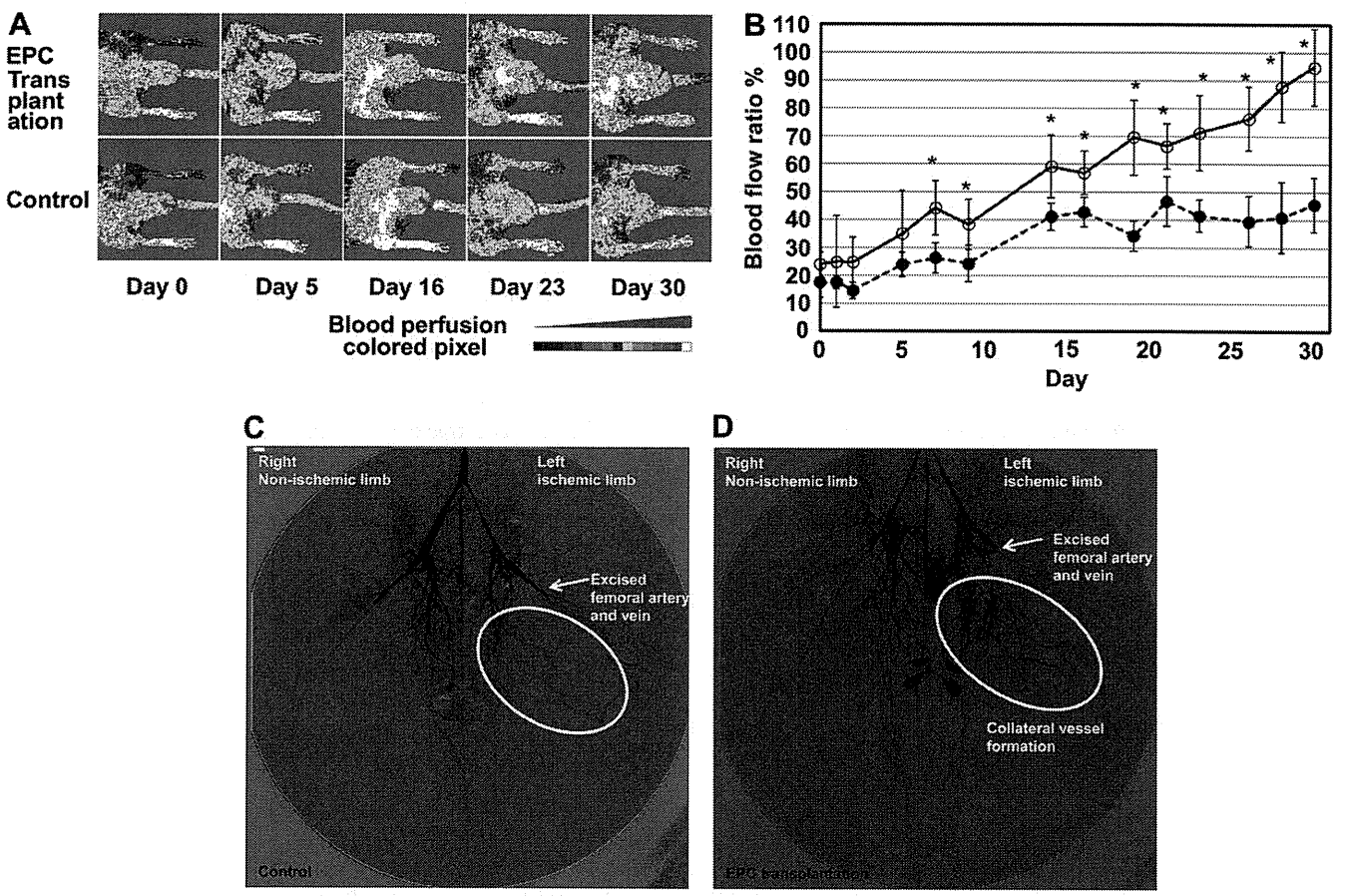

Fig. 2. Recovery of blood flow in ischemic limbs measured by using a Laser Doppler Perfusion Imager (LDPI). (A) A greater blood perfusion signal (red to white) was observed in the ischemic area where EPCs were transplanted. Blood flow ratio = cell flux/normal flux (B) Representative LDPI. Dex-DOTA-Gd^{3+} labeled EPCs transplanted into the ischemic limb (●, $n = 6$), control, non-labeled Dex-DOTA-Gd^{3+} cells (○, $n = 6$), values are mean (±SD) at each time point. $P > 0.05$ and $^*P < 0.001$ vs. control. (C) Representative angiograms of the non-ischemic limb model injected only with Bolheal® (control), and (D) rat ischemic limb model injected with 20×10^6 Dex-DOTA-Gd^{3+}-labeled EPCs in Bolheal® (EPC transplantation). Angiograms were performed after injection of the contrast agent (iodone) through a catheter inserted in the abdominal aorta ($n = 3$/group). Videos of the ischemic model after labeled cell implantation (video 1) and after 14 (video 2) are available as electronic supplementary data. (For interpretation of the references to colour in this figure legend, the reader is referred to the web version of this article.)

3D-Doctor software. The white and deep red colors represent the volume occupied by labeled cells (Fig. 3B and C, and Fig. 4). Consistent with the results shown in Supplementary Fig. 2, rendered MRIs obtained from the T1-weighted images (total 35) clearly exhibited the migration pattern of labeled EPCs in the ischemic limb. In contrast, MRIs of Dex-DOTA-Gd^{3+}-labeled EPCs transplanted into non-ischemic rat models showed the presence of transplanted cells in the muscle (Fig. 3C), but no significant movement was observed and cells gradually disappeared within 8 days post-transplantation. T1-weighted images of the non-ischemic limb confirmed the low capacity of cells to migrate.

Moreover, in a separate experiment, T2*-weighted images identified SPIO-labeled EPCs in the ischemic limbs (Supplementary Fig. 4). The area of MRI contrast appears to be extended in the limb. This could be partly due to the sensitivity of T2* imaging, which could induce disturbances in the magnetic field causing an amplification of the signal. However, SPIO-labeled cells seemed to remain static and detectable in the ischemic limb without apparent migration or loss of signal from the transplantation point after 21 days. The 3D rendered images better illustrate this behavior exhibited by SPIO-labeled cells (Fig. 4A).

One of the features of the 3D-Doctor software is that it enables the measurement of the volume occupied by the implanted labeled cells in the tissue. The volume of cells in the limb calculated with this software is shown in Figs. 3D and 4B. In all models, the volume of labeled implanted cells was around 500 mm^3. In the ischemic model, the volume of Dex-DOTA-Gd^{3+}-labeled EPCs increased while the cells were migrating, reaching a maximum value (2706 mm^3) at day 6 followed by a decrease due to the reduction of the signal of the contrast agent until day 16. In the non-ischemic model, on the other hand, the volume of the Dex-DOTA-Gd^{3+}-labeled EPCs barely increased on day 2 and rapidly diminished on day 8. This result is in disagreement with that obtained with SPIO-labeled EPCs, in which the volumes were not statistically different from day 1 until day 21 post-transplantation ($P > 0.05$).

3.4. Gadolinium clearance from the body

We first quantified the total amount of Gd in the transplanted labeled EPCs in the ischemic and non-ischemic models by ICP mass. After electroporation, we found that 1 EPC contained 0.83 pg of Gd for a total of 7.78 ± 0.73 μg Gd/rat transplanted in the limb (1.65×10^{-4} mmol/kg body weight [BW]). This dose was significantly lower (1814 times) than the average contrast material dosage used for human patients (0.3 mmol/kg BW = 18 mmol) [39].

Urine and feces were separately collected every 48 h from the metabolic cages in which ischemic and non-ischemic rat models were placed. After treatment with nitric acid, the quantity of Gd was measured by ICP mass. The percentage of Gd excreted from the rats in correlation to the total dose applied is shown in Fig. 5. Two different clearance profiles were observed in the samples. The total amount of Gd cleared from the non-ischemic rat models was 74% (5.73 μg) compared to 43% (3.4 μg) cleared in the ischemic model (Fig. 5). In both cases, Gd was gradually cleared via urine and feces until day 14, and the Gd clearance was suspended until day 20. Although the percentages of Gd excreted from the 2 rat models were not statistically different until day 6, significant differences in Gd clearance were revealed after day 8. Rat ischemic models cleared approximately 32% of the total Gd applied via the urine (2.49 μg), in contrast to non-ischemic rat models, in which 47% of the total Gd dose (3.67 μg) were cleared via urine. Similar results were obtained with regard to the Gd clearance via feces, in which the non-ischemic models cleared an additional 27% (2.06 μg) in comparison to the ischemic models (12%, 0.93 μg).

To further investigate whether the remaining Gd could be accumulated in different target organs, liver, lungs, and kidneys of the rat models were excised and treated with nitric acid to quantify the Gd using ICP mass (Supplementary Table 2). The results showed that Gd did not accumulate in the lungs of any of the rat models. However, a small amount of Gd was found in kidneys and livers from both rat models. The cumulative dose percentage of Gd in the kidneys of ischemic models was $7.4 \times 10^{-4} \pm 2.9 \times 10^{-4}$% (60.5 pg) and $9.1 \times 10^{-4} \pm 2.1 \times 10^{-4}$% (66.2 pg) in non-ischemic rats. The percentage of Gd in the livers was $8.9 \times 10^{-4} \pm 2.1 \times 10^{-4}$% (72.9 pg) and $9.9 \times 10^{-4} \pm 2.1 \times 10^{-4}$% (72.1 pg) for the ischemic and non-ischemic models, respectively.

3.5. Histological assessment of cell engraftment

In all animals implanted with SPIO, Berlin blue-positive cells were detected at the injection site in tissue sections (Fig. 6). To identify the iron-containing cells, sections adjacent to those exhibiting Berlin blue-positive cells from all rats killed at day 21 were tested for a macrophage-specific antigen (CD68 or macrosialin) by immunocytochemistry, which revealed several CD68-positive cells, with a staining pattern similar to that seen with Berlin blue-positive cells (Fig. 6A and B).

Moreover, sections corresponding to the Berlin blue-positive areas were tested for the presence of a specific EPC marker (vWF) and a negative marker (α-SMA).

Staining for vWF exposed many positive areas (brown color in Fig. 6C) in the sections derived from animals sacrificed at 21 days, and a similar pattern was obtained with α-SMA (brown color in Fig. 6D), which likely shows that EPCs already differentiated into the endothelial phenotype. This pattern, however, differed from that observed with Berlin blue. These results confirm the discordance between the MRI signal and the SPIO-labeled EPCs.

4. Discussion

The present findings revealed important characteristics of Dex-DOTA-Gd^{3+} as MRI contrast agent for stem cell therapy by identifying features of angiogenesis of ischemic tissues after transplantation of labeled EPCs that could have significant clinical and research implications. First, the reliability of Dex-DOTA-Gd^{3+} for the detection and tracking of living labeled EPCs by MRI for long periods was demonstrated. In addition, the clearance of free contrast agent, which was likely released from dead cells, via urine and feces was shown. Second, Dex-DOTA-Gd^{3+} can provide fundamental information on the migration phenomena likely caused by chemoattraction or paracrine effects to ensure proper incorporation at the site of revascularization of ischemic tissues. In addition, we examined the ability of SPIO as an MRI contrast agent for the tracking of labeled EPCs. A persistent MRI signal from the ischemic limbs after transplantation of SPIO-labeled EPCs might be the result of phagocytosis of iron nanoparticles by resident macrophages. Our findings showed the limitations of SPIO labeling methods in preclinical and clinical trials of stem cell therapy.

Preclinical studies have indicated that ex vivo EPC transplantation could be used to promote neovascularization of ischemic tissues by showing the augmentation of naturally impaired neovascularization in an animal model of induced ischemic limb [40,16]. Asahara et al. [15], reported that intravenously transfused EPCs contribute to neovascularization of ischemic tissues in an adult experimental animal. In a different study, BM-derived EPCs were shown to home and incorporate into the sites of vasculogenesis [1,37].

In a recent publication from our group [35], we described the synthesis and properties of Dex-DOTA-Gd^{3+} as an MRI contrast

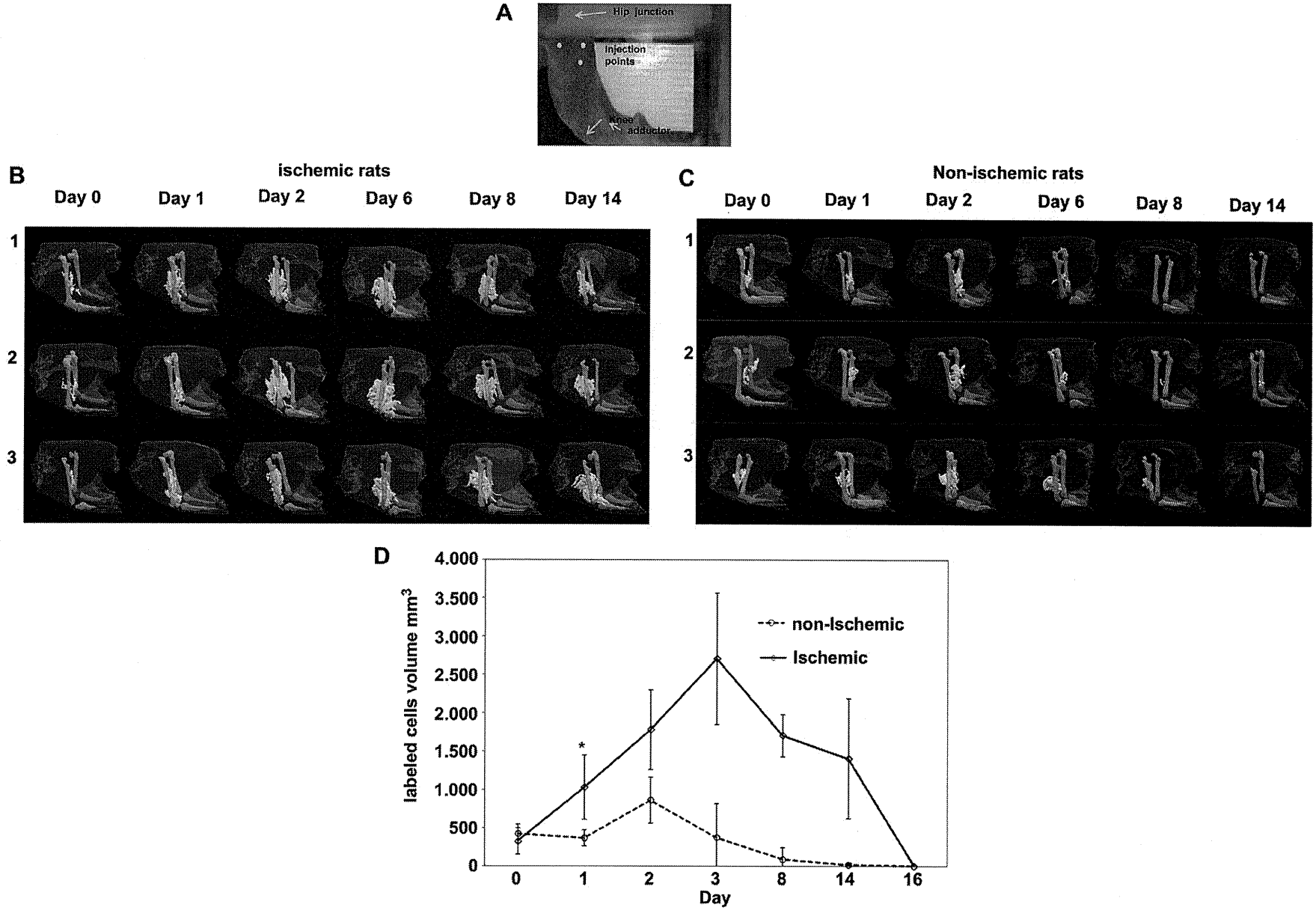

Fig. 3. Three-dimensional reconstructed MRIs of Dex-DOTA-Gd^{3+} labeled EPCs after intramuscular injection in ischemic limb rat models. (A) Rat position in the MRI indicating the injection points in the limb. (B) MRIs of the labeled EPC migration pattern in the ischemic limb in a rat ischemic limb model (F344, male, 8 weeks old, total 3 rats) in the inguinal region where the femoral artery and vein were excised. (C) Dex-DOTA-Gd^{3+}labeled EPC in non-ischemic models (total 3 rats). (D) Volume occupied by the implanted labeled cells in the tissue, as calculated using 3D-Doctor. Values represent mean (±SD) at each time point ($n = 3$/group). No statistically significant differences were detected between the ischemic and non-ischemic models after labeled cell transplantation at day 0, $^*P > 0.05$, while statistically significant differences were noted from days 1–14, $^*P < 0.001$. Overall, the different pattern of migration in the ischemic and non-ischemic models was due to the absence of released chemokines, which are known to mobilize EPCs, in response to vascular injury.

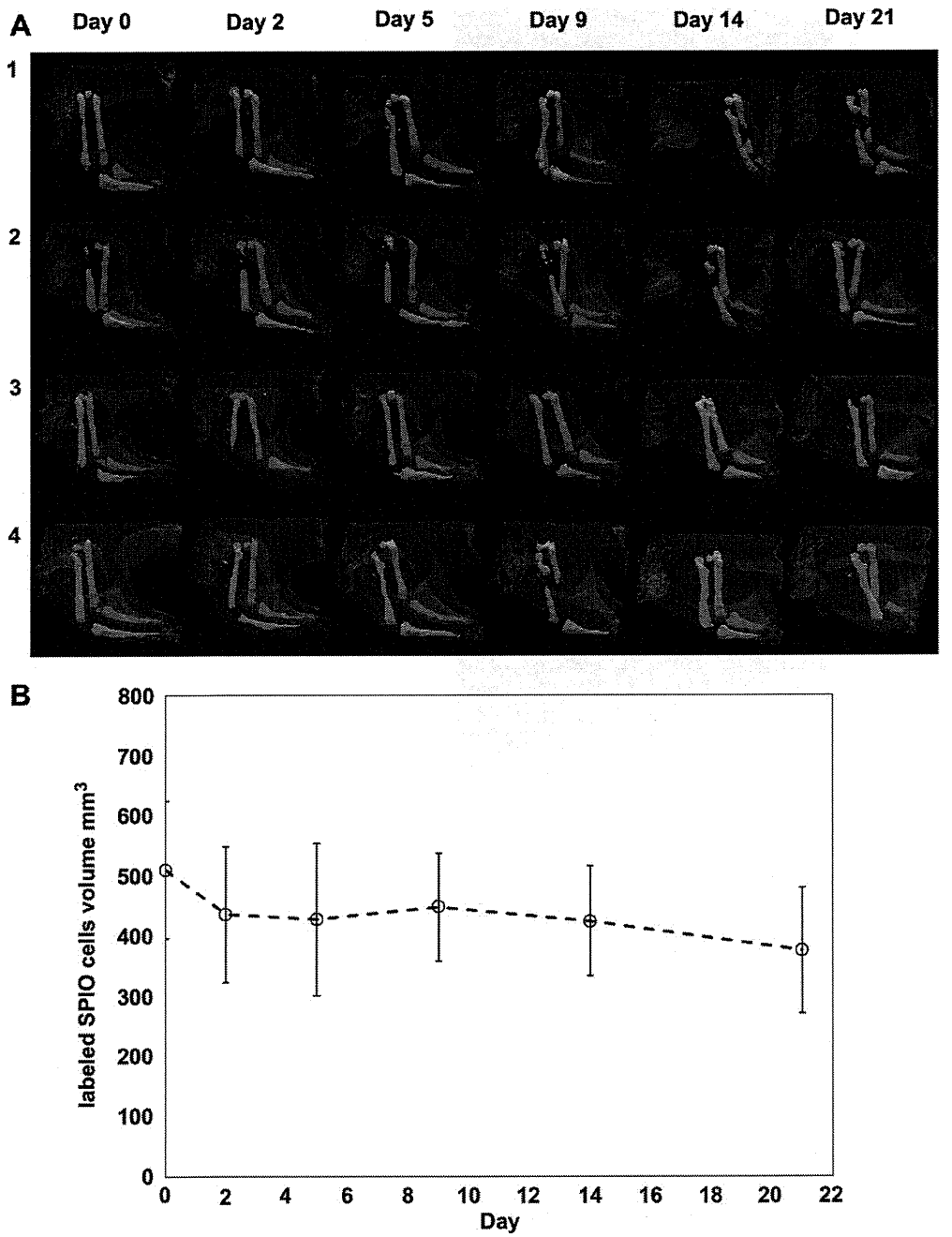

Fig. 4. Three-dimensional reconstructed (MRIs) of SPIO-labeled EPCs after intramuscular injection in rat ischemic limb models. (A) MRIs of SPIO-labeled EPCs in ischemic models (total 4 rats). (B) Volume occupied by the implanted labeled cells in the tissue calculated using 3D-Doctor. Values represent mean (±SD) at each time point ($n = 4$). No statistically significant differences were detected between day 0 and day 21 after labeled cell implantation. $P > 0.05$. Note the lack of migration in SPIO signal and the unviable volume in the ischemic model.

agent that satisfied certain conditions such as the provision of desired MRI contrast properties, ex vivo cell labeling before transplantation, highly sensitive and stable intracellular labeling (Fig. 1B and C), biocompatibility without affecting cell viability, proliferation or healing capacity by enhancing capillary formation, and the maintenance of consistently detectable signals for long periods of time. We also demonstrated that Dex-DOTA-Gd^{3+} was not taken up by resident macrophages and we double stain the Dex-DOTA-Gd^{3+} labeled EPC by Qtracker® 655. EPCs were localized in the neovascular zones of the ischemic limb ensuring that MRI signals correspond to signals generated by the labeled cells. In the present study, we assessed whether Dex-DOTA-Gd^{3+} has any adverse effects on the capacity of EPCs to release grow factors and promote angiogenesis and vasculogenesis in a rat ischemic limb model. The Dex-DOTA-Gd^{3+} labeled EPC were found that this labeling process (electroporation) barely affected the cell's biological properties. After, labeling, EPC continue to divide and proliferate as non-labeled cells. The expression of EPC membrane proteins was not statistically modified by the labeling (Fig. 1E). In particular, the expression of two adherence proteins, PECAM-1 and VE-cadherin